LA-13240-MS

Response of a Water-Filled Spherical Vessel to an Internal Explosion

Los Alamos
NATIONAL LABORATORY

Los Alamos National Laboratory is operated by the University of California for the United States Department of Energy under contract W-7405-ENG-36.

This work was supported by the U.S. Department of Energy and the U.S. Department of Defense.

An Affirmative Action/Equal Opportunity Employer

LA-13240-MS

UC-000
Issued: June 1997

Response of a Water-Filled Spherical Vessel to an Internal Explosion

M. W. Lewis
T. L. Wilson

Los Alamos
NATIONAL LABORATORY
Los Alamos, New Mexico 87545

Section **CONTENTS** **Page**

Response of a Water-Filled Spherical Vessel to an Internal Explosion

M. W. Lewis
and
T. L. Wilson

ABSTRACT

We model the response of a water-filled, thick-walled, spherical steel vessel to an internal explosion of 30 grams of C-4 with FSI2D—a two-dimensional coupled finite element and finite volume hydrodynamics code. The gas phase detonation products were modeled with a Becker-Kistiakowsky-Wilson high-explosive equation of state.

Predictions from a fully coupled model were compared to experimental results in the form of strain gauge traces. Agreement was reasonably good. Additionally, the calculation was run in an uncoupled mode to understand the importance of fluid-structure interaction in this problem. The uncoupled model results in an accumulation of nonphysical energy in the vessel.

I. INTRODUCTION

Many problems of interest to the defense community involve fluid-structure interaction (FSI). Such problems include underwater blast loading of structures, bubble dynamics and jetting around structures, and hydrodynamic ram events. These problems may involve gas, fluid, and solid dynamics, nonlinear material behavior, cavitation, reaction kinetics, material failure, and nonlinearity that is due to varying geometry and contact conditions within a structure or between structures.

We developed an approach for modeling such problems by coupling existing analysis codes, each of which models one of the two domains, the fluid or the structure. We implemented this approach for modeling two-dimensional problems by coupling MFICE2D and the CFDLIB family of codes [1, 2], a LANL finite volume computation fluid dynamics (CFD) code, with PRONTO2D [3], a SANDIA finite element solid dynamics code. Details on this coupling approach and current implementations are discussed in Section III.

This reports describes an application of this coupled code. We used the code to model an experiment conducted by Larry Hull and others in the Dynamic Experimentation (DX) Division in support of a reactive munitions project. The problem involves the detonation of 30 grams of high explosive, C-4, in the center of

a water-filled, thick-walled, nearly spherical steel vessel (hereafter called the Jumbino vessel). The vessel was instrumented with eighteen strain gauges.

Two new features of the code were used in modeling this problem. We have a new energy partition calculation that calculates how much work is done on the structure and the current total energy in the fluid and solid domains. This calculation may be used to measure the effectiveness of a certain explosive configuration or some other method of delivering energy through a fluid to a target structure.

Another new feature demonstrated for this problem is the capability of running a problem both in a strongly coupled mode and in an uncoupled mode. In the strongly coupled mode, where the particle normal velocity is continuous across the interface, an iterative approach is used to force the pressure field and the structural accelerations to be compatible. In this mode, the physical fluid-structure interface moves; that is, the fluid domain changes as the structure deforms, translates, and rotates. Momentum and energy are conserved. In the uncoupled mode, the fluid-structure interface is treated as a rigid boundary when the fluid equations are solved. Pressures so calculated are then used as boundary conditions to the structure, which then deforms, translates, and rotates. Momentum and energy are *not* conserved.

II. PROBLEM DESCRIPTION

A drawing of the Jumbino vessel is shown in Fig. 2.1. One end of the vessel (the right end in the figure) was sealed with a one inch thick Plexiglas plug. A steel plug was bolted in the other end as shown in the figure. The vessel is made of A537 structural steel, with an estimated yield strength of 40,000 psi.

The vessel was supported by a rectangular steel frame with clamps around each end of the vessel. The frame is shown in Fig. 2.2. This support arrangement makes the problem slightly asymmetric.

Thirty grams of C-4 were detonated at the center of the vessel. The charge was a cylindrical charge with a diameter of 1.00 in. and a length of 1.413 in. A polyvinyl chloride (PVC) pipe with holes drilled through its walls at several locations was used to hold the high explosive (HE) and detonator arrangement.

One-quarter inch strain gauges were placed on the outside of the vessel to record the azimuthal and meridional components of the vessel motion. These strains, referred to here as the hoop and longitudinal components, respectively, are principal strains in an ideally axisymmetric problem. Gauges were affixed at seven locations along the $\theta = 0$ meridian at 15° ϕ intervals from -45° to +45° and at three locations around the equator ($z = 0$) at 120° θ intervals as indicated in Fig. 2.3.

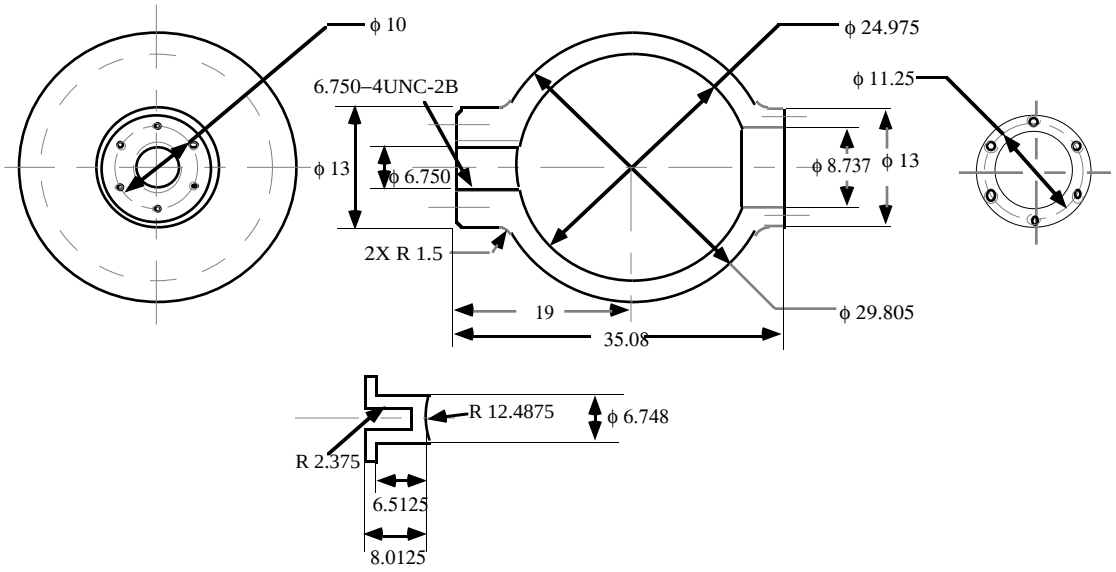

Fig. 2.1 Engineering sketch of the Jumbino vessel. The steel plug inserted into the left (as shown) end is shown below the sketch. All dimensions are in inches.

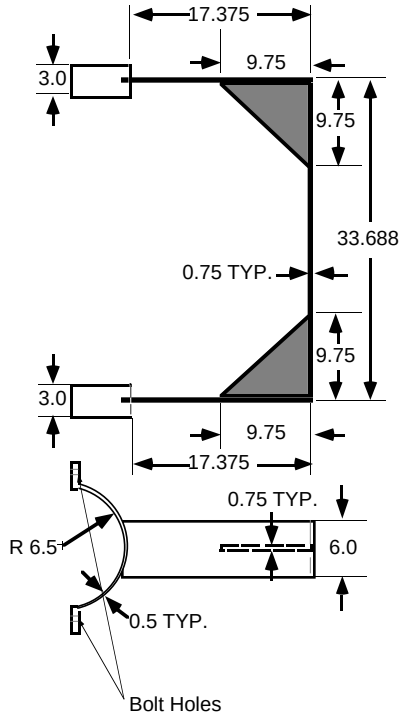

Fig. 2.2 A sketch of the right half of the support structure used to hold the Jumbino vessel. Unless otherwise noted, all parts are welded. The structure was supported at the midpoint of the 33.7 in. long plate on the right. The vessel was attached to the structure by the bolted clamps shown. All dimensions are in inches.

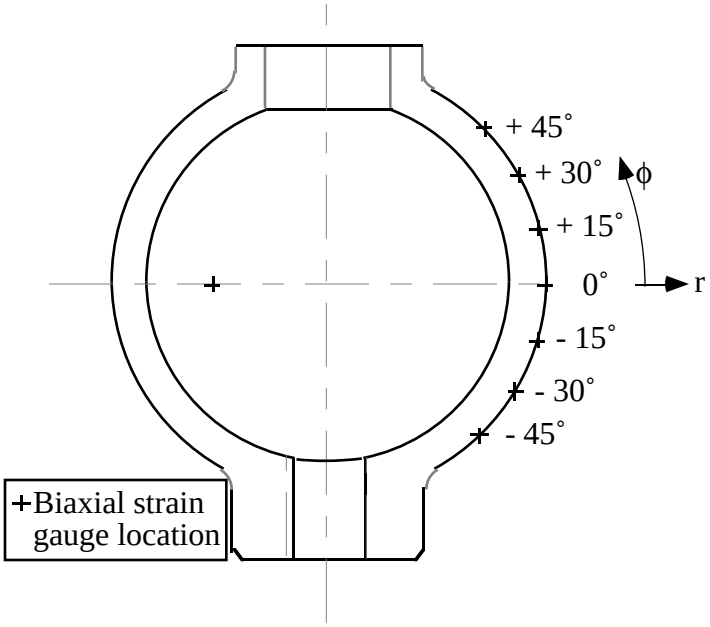

Figure 2.3 An engineering sketch of the Jumbino vessel indicating strain gauge locations. Two strain gauges were at each location shown, one latitudinal (or hoop) gauge and one longitudinal gauge.

III. NUMERICAL FSI METHODOLOGY

A fully implicit numerical coupling of the fluid and solid solutions facilitates a physically coupled solution. In this section we describe the FSI portion of the solution algorithm following the discussion given by Lewis et al. [4]. The full CFD algorithm is discussed in Kashiwa et al. [1, 2] and details of the solid dynamics algorithm are discussed in Taylor and Flanagan [3].

Nodes on the surface of the structural domain are required to be coincident with vertices on the surface of the fluid domain. Pressure and velocity data are exchanged on the faces defined by these points and at these points.

Let **u** be the vector of velocities that defines the motion on the structural and fluid domains. Consider a subset of the equations of motion given by

$$\dot{\mathbf{u}} = -\nabla p \,, \tag{3.1a}$$

and

$$\dot{p} = -\rho c^2 \nabla \cdot \mathbf{u} \,, \tag{3.1b}$$

where ρ is the local density. A typical discretization is given by

$$\Delta \mathbf{u} \;=\; -G[\mathrm{p}^{\mathrm{n}} + \Delta \mathrm{p}] \;, \tag{3.2a}$$

and

$$\Delta \mathrm{p} \;=\; -D[\mathbf{u}^{\mathrm{n}} + \Delta \mathbf{u}] \;, \tag{3.2b}$$

where the standard superscript notation is used for time increment and where G and D are discrete gradient and divergence operators, respectively.

The typical solution scheme comes from eliminating $\Delta\mathbf{u}$ between these equations and solving for Δp. That is,

$$[I + DG]\Delta \mathrm{p} \;=\; -D[\mathbf{u}^{\mathrm{n}} - G[\mathrm{p}^{\mathrm{n}}]] \;, \tag{3.3}$$

where I is the identity operator. The operator $[I + DG]$ is usually sparse, and the solution can be obtained by any of a variety of linear system solvers. Having found Δp everywhere, back substitution into Eq. (3.2a) gives $\Delta\mathbf{u}$ that is guaranteed to be stable for any value of $c\Delta t / \Delta x$. This is the essence of the cell-centered implicit continuous Eulerian (ICE) CFD method.

In our case we have elected to connect the structural domain to the fluid domain by way of boundary data transfer, so the elimination step and subsequent global solution for Δp is not possible. Nevertheless, we must retain the discretization given by Eqs. (3.2) to achieve a robust method. This is done as follows.

Let subscripts s, f, and b denote values of the field variables in the structural domain, the fluid domain, and points along the common boundary, respectively. Now we may write

$$\Delta \mathrm{p}_{\mathrm{f}} \;=\; -D[\mathbf{u}_{\mathrm{f}}^{\mathrm{n}} - G[\mathrm{p}_{\mathrm{f}}^{\mathrm{n}} + \Delta \mathrm{p}_{\mathrm{f}}]] - D_b[\mathbf{u}_{\mathrm{s}}^{\mathrm{n}+1}] \;, \tag{3.4a}$$

and

$$\Delta \mathbf{u}_{\mathrm{s}} \;=\; -G[\mathrm{p}_{\mathrm{s}}^{\mathrm{n}} - D[\mathbf{u}_{\mathrm{s}}^{\mathrm{n}} + \Delta \mathbf{u}_{\mathrm{s}}]] - G_b[\mathrm{p}_{\mathrm{f}}^{\mathrm{n}+1}], \tag{3.4b}$$

where we extract from D and G those operators that act only on the boundary values, D_{b} and G_{b}. A successive substitution method can be used to find $\mathbf{u}_{\mathrm{s}}^{\mathrm{n}+1} = \mathbf{u}_{\mathrm{s}}^{\mathrm{n}} + \Delta \mathbf{u}_{\mathrm{s}}$ and $\mathrm{p}_{\mathrm{f}}^{\mathrm{n}+1} = \mathrm{p}_{\mathrm{f}}^{\mathrm{n}} + \Delta \mathrm{p}_{\mathrm{f}}$. The successive substitution procedure follows. Let

$$\mathbf{u}_{\mathrm{s}}^{0} \;=\; \mathbf{u}_{\mathrm{s}}^{\mathrm{n}} \;, \tag{3.5a}$$

and

$$p_f^0 = p_f^n , \tag{3.5b}$$

and iterate in the following manner:

$$[I + DG]\Delta p_f^{k+1} = -D[\mathbf{u}_f^n - G[p_f^k]] - D_b[\mathbf{u}_s^k] \tag{3.6a}$$

$$p_f^{n+1} = p_f^n + \alpha^{k+1}\Delta p_f^{k+1} \tag{3.6b}$$

$$[I + GD]\Delta \mathbf{u}_s^{k+1} = -G[p_s^n - D[\mathbf{u}_s^n]] - G_b[p_f^{k+1}] \tag{3.7a}$$

$$\mathbf{u}_s^{n+1} = \mathbf{u}_s^n + \beta^{k+1}\Delta \mathbf{u}_s^{k+1} \tag{3.7b}$$

for k = 0, 1, 2, 3, ..., until Δp and $|\Delta \mathbf{u}|$ are small compared with norms $\|p_b\|$ and $\|\mathbf{u}_b\|$. Here α^k and β^k are under-relaxation parameters [4]. Notice that Eq. (3.6a) is solved in the fluid domain with an explicit source term coming from the previous iterate boundary velocity. The update Eq. (3.6b) uses fluid field pressure data from Eq. (3.6a). Then Eq. (3.7a) is solved in such a way that the current iterate pressure forms an explicit source to the structural domain. Finally, the boundary velocity is updated and becomes the source for the next fluid domain pressure solution.

IV. COMPUTATIONAL MODEL

A. Fluid Domain. An axisymmetric cylindrical coordinate system is used to describe the geometry of the Jumbino experiment where (r, θ, and z) are the radial, azimuthal, and axial coordinates that form a right-handed coordinate system. The angle ϕ, measured counterclockwise from the r-axis in the meridional plane, denotes the angle of latitude.

The interior of the vessel, known hereafter as the fluid domain, contains an undeformed volume of 1.41328 x 10^5 cm^3 initially filled with water and fitted with a 30 g charge of C-4 high explosive at the spherical center. The fluid domain, shown in Fig. 4.1, is discretized with 4279 quadrilateral cells, ranging in size from 0.42 by 0.42 cm at the center to 0.85 by 0.85 cm at the vessel wall, in eight logically rectangular blocks.

At the instant of detonation, the water is motionless and in hydrostatic equilibrium with the ambient atmosphere. A Us-Up equation of state is used to model the water [5, p. 391]. For the high explosive, a Becker-Kistiakowsky-Wilson (BKW)-gas is given the initial conditions $\rho = \rho_o = 1.65\ g/cm^3$, T = 2714.16 K, and p = 152.7 kbars, simulating the mass and energy of the explosive. Properties of C-4 are given in Appendix A, and details of the BKW-gas equation of state are given in Appendix B.

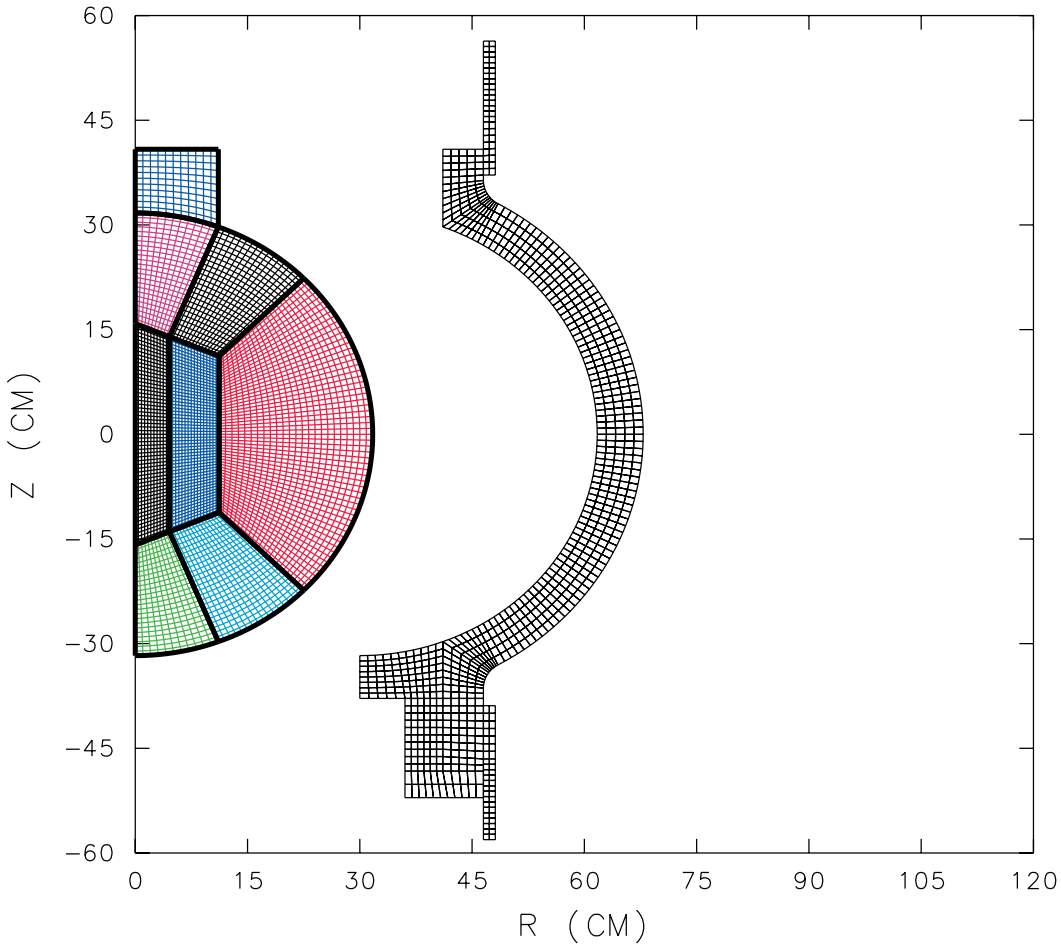

Fig. 4.1
Computational mesh for fluid and solid domains.

Boundary conditions are straightforward. Along the z-axis the axisymmetric condition is modeled as a reflective surface, the water-Plexiglas interface at the top of the port is modeled as an outflow (zero normal gradient) surface and the water-vessel interface is modeled with the FSI model described in Section III.

B. Jumbino Vessel. The vessel, shown radially offset from the fluid in Fig. 4.1, is discretized with 765 quadrilateral finite elements. A typical element dimension is 1 cm. The vessel steel properties are density = 7.833 g/cm^3, Young's modulus of elasticity = 2.07 x 10^6 bars, Poisson's ratio = 0.29, and uniaxial yield stress = 2760 bars. This was modeled as an elastic-plastic material with isotropic hardening. The hardening modulus was 9410 bars.

Compliance of the support structure is modeled by including elements that provide an additional mass of 1.997 kg and an axial stiffness of 30.873 x 10^4 N/cm. The axial

displacements of the lowermost and uppermost nodes of the support structure model were constrained to be zero. The clamps around each end of the vessel were modeled as steel, 1.5875 cm (5/8-in.) thick and 7.62 cm (3.0 in.) long, with the same material properties as those of the vessel. The clamps were modeled as axisymmetric and rigidly welded to the vessel and the support structure.

V. ONE-DIMENSIONAL SHELL DYNAMICS

Because the Jumbino experiment is nearly spherically symmetric, its essential features may be examined as a function of radius and time. In this section we develop two simplified models that predict the coupled and uncoupled vessel dynamics that accompany a specified pressure loading, p(t), on the inner surface. The form of p(t), discussed in the Section V.A, approximates the initial water shock wave.

Vessel energy and hoop strains, given in Sections V.B and V.C, illustrate the essential FSI features that are discussed more fully with the FSI2D calculations in Section VI.

A. Underwater Shock Wave Parameters. After the underwater detonation of a high-explosive charge, the ensuing motion may be understood in terms of the dynamics of the gas-phase explosive products (hereafter referred to as the bubble) and the motion of the water. If the explosive is compact, that is, does not differ in shape significantly from a sphere or a cube, the physics may be adequately studied in terms of spherical radius and time only. In the absence of nearby solid boundaries or free surfaces, the bubble expands until its pressure is substantially less than that of the surrounding water; that is, it overshoots equilibrium. The bubble then contracts to a new minimum radius and maximum pressure before the process starts again. The series of bubble oscillations drive an ever weakening series of shocks and acoustic pulses into the water.

The dynamics of underwater explosions has been studied experimentally and theoretically since World War II [6-8]. From dimensional considerations it may be shown that properties of the first shock wave may be studied in terms of the charge weight (W) and distance from the explosion (r). Experimental evidence further indicates that several parameters are well represented by equations of the form

$$\text{Parameter} = K\left(\frac{W^{1/3}}{r}\right)^{\alpha}, \tag{5.1}$$

where α and K depend on the explosive. Swisdak [8] gives the following correlations for TNT:

$$p_m = 134.9\left(\frac{W^{1/3}}{r}\right)^{1.13} \tag{5.2}$$

$$\theta / W^{1/3} = 4.946 \times 10^{-3} \left(\frac{W^{1/3}}{r} \right)^{-0.23} \tag{5.3}$$

$$I / W^{1/3} = 44.634 \left(\frac{W^{1/3}}{r} \right)^{0.89} \tag{5.4}$$

$$e_f / W^{1/3} = 925.43 \left(\frac{W^{1/3}}{r} \right)^{2.04}, \tag{5.5}$$

where p_m is the maximum pressure, θ is the time required for the pressure to fall to $1/e$ (37%) of p_m, I is the impulse per unit area and e_f is the energy flux density. Constants on the right side of Eqs. (5.2)-(5.5) have been changed so that dimensional units are consistent with the present report.

The Jumbino experiment is complicated by multiple wave interactions because waves reflect inward from the vessel and outward from the bubble; however, because the first shock travels in unperturbed water, its properties should be adequately described by Eqs. (5.2)-(5.5). Solving these equations at the moment of impact ($r = R_i$) yields $p_m = 576.8$ bars, $\theta = 0.0284$ ms, $I = 21.413$ bar-ms, and $e_f = 34.66$ bar-cm. The value of W in Eqs. (5.2)-(5.5) is modified to account for the difference in the energy of detonation between C-4 (1400 cal/g) and TNT (1020 cal/g);

$$W = (30\ g)(1400/1020) = 41.176g\ . \tag{5.6}$$

B. Acoustic Model. To estimate the energy transmitted to the vessel, E_t, we model the incident shock as an acoustic wave. This approximation is justified because $(p_m - p_o)/(\rho_o c_o^2) = 0.026 << 1$. Then, when we consider the shock-vessel impact as an acoustic wave transmission problem, the fraction of the incident shock energy reflected back into the water is

$$E_r = \left(\frac{\Re_2 - \Re_1}{\Re_2 + \Re_1} \right)^2 = \left(\frac{\rho_s c_s - \rho_o c_o}{\rho_s c_s + \rho_o c} \right)^2 = 0.863, \tag{5.7}$$

and the fraction transmitted to the vessel is

$$E_t = 1 - E_r = 0.137, \tag{5.8}$$

where $\Re_1 = \rho_o c_o$ and $\Re_2 = \rho_s c_s$ are the acoustic impedances for the water and vessel respectively.

In the context of FSI, Eqs. (5.7) and (5.8) correspond to the coupled case where energy and momentum are conserved. In the uncoupled case, the reflected fluid wave is identical to the incident wave being computed from a rigid boundary condition. Thus, uncoupled FSI is not conservative because, by definition, momentum and

energy gained (lost) by the vessel is not lost (gained) by the fluid. The transmitted energy for the uncoupled case is then

$$E_{t_{uncoupled}} = \frac{E_{r_{uncoupled}}}{E_{r_{coupled}}} E_{t_{coupled}} = \frac{1.000}{0.863} 0.137 = 0.1587. \quad (5.9)$$

For an incident shock with energy E_i, Fig. 5.1 shows the partition of energy for the uncoupled and coupled approximations.

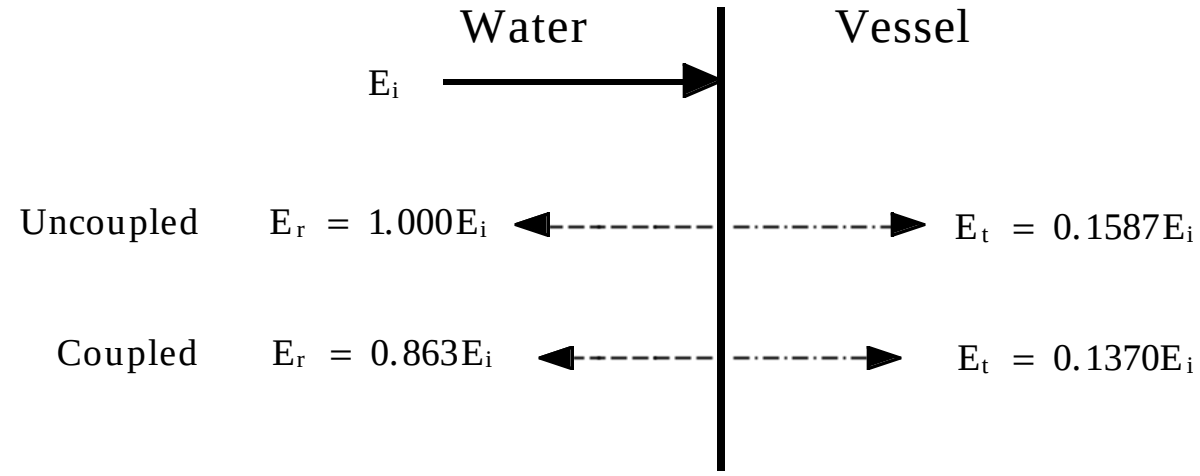

Fig. 5.1
Incident, reflected, and transmitted energy when the first shock is considered as an acoustic wave.

When we use the results of Eqs. (5.5) and (5.9), the total energy transmitted to the vessel by the shock is

$$E_{t_{coupled}} = 0.137 e_f A_i = 6.003 \times 10^4 \text{ bar} - \text{cm}^3, \quad (5.10)$$

and

$$E_{t_{uncoupled}} = 0.1587 e_f A_i = 6.954 \times 10^4 \text{ bar} - \text{cm}^3. \quad (5.11)$$

The maximum hoop strain in the spherical shell is

$$\varepsilon_{max} = \left[\frac{E_t (1-\nu)}{V_s Y} \right]^{1/2} = 4.69 \times 10^{-4} (\text{coupled}), 5.05 \times 10^{-4} (\text{uncoupled}) . \quad (5.12)$$

Thus, the vessel in the uncoupled case receives 15.8% more energy and has 7.7% higher peak strains than does the coupled case.

C. Shell Dynamics Model. Consider the motion of the vessel caused by the initial shock loading. The equation of motion for a moderately thick-walled elastic spherical shell is

$$\ddot{s} = \frac{R_r^2 p(t)}{\rho_s h} - \frac{2\sigma}{\rho_s R}, \tag{5.13}$$

where s is the radial shell displacement measured from the inner surface, σ is the biaxial hoop stress, $R \equiv \left(R_i + R_o\right)/2$ is the mean shell radius, ρ_S is the shell density, and $R_r \equiv R_i / R$.

The incident pressure $p_1(t)$ and the reflected pressure $p_2(t)$ are modeled as acoustic plane waves; thus,

$$p(t) = p_1(t) + p_2(t). \tag{5.14}$$

The corresponding particle velocities are

$$u_1 = p_1 / \rho_o c_o, \tag{5.15a}$$

and

$$u_2 = -p_2 / \rho_o c_o. \tag{5.15b}$$

At the surface, the water and the vessel have the same velocity; hence, the shell boundary conditions are

$$u = 0 \quad \text{at } (s = 0, t = 0) \tag{5.16a}$$

and

$$u = u_1 + u_2 \quad \text{at } (s = 0, t). \tag{5.16b}$$

It has been empirically established that the shock wave pressure decays nearly exponentially. If $p_1(t) = p_m e^{-t/\theta}$, Eq. (5.14) becomes

$$p(t) = 2p_m e^{-t/\theta} - \rho_o c_o u \quad \text{(coupled)}, \tag{5.17a}$$

or

$$p(t) = 2p_m e^{-t/\theta} \quad \text{(uncoupled)}. \tag{5.17b}$$

Figure 5.2 shows these two pressure functions.

Equation (5.13) may now be written as

$$\ddot{s} + \frac{2\beta}{\theta}\dot{s} + \omega^2 s = \frac{2R_r^2 p_m}{\rho_s h} e^{-t/\theta} \quad \text{(coupled)}, \tag{5.18a}$$

and

$$\ddot{s} + \omega^2 s = \frac{2R_r^2 p_m}{\rho_s h} e^{-t/\theta} \quad \text{(uncoupled)}, \tag{5.18b}$$

where

$$\omega^2 \equiv \frac{2\sigma}{\rho_s h} = \frac{2Y}{\rho_s R^2 (1-\nu)}, \tag{5.19a}$$

and

$$\beta \equiv \frac{R_r^2 \rho_o c_o \theta}{2\rho_s h}. \tag{5.19b}$$

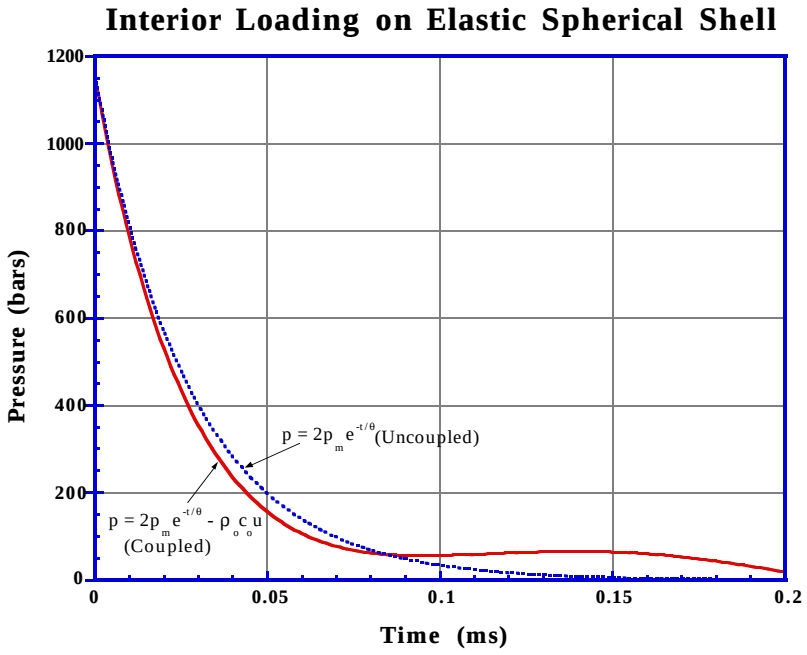

Fig. 5.2
Coupled and uncoupled pressure loading.

The general underdamped solution for Eqs. (5.18a) and (5.18b) yields the following expressions for the coupled and uncoupled velocity and displacement.

Coupled.

$$u = \frac{2R_r^2\theta p_m}{\rho_s h\left(\omega^2\theta^2 - 2\beta + 1\right)}\left\{e^{-\beta t/\theta}\left[(\theta\phi + \beta(\beta-1)/\theta\phi)\sin\phi t + \cos\phi t\right] - e^{-t/\theta}\right\} . \quad (5.20a)$$

$$s = \frac{2R_r^2\theta^2 p_m}{\rho_s h\left(\omega^2\theta^2 - 2\beta + 1\right)}\left\{e^{-\beta t/\theta}\left[\frac{(1-\beta)}{\theta\phi}\sin\phi t - \cos\phi t\right] + e^{-t/\theta}\right\} . \quad (5.20b)$$

Uncoupled.

$$u = \frac{2R_r^2\theta p_m}{\rho_s h\left(\omega^2\theta^2 + 1\right)}\left\{\omega\theta\sin\omega t + \cos\omega t - e^{-t/\theta}\right\} . \quad (5.20c)$$

$$s = \frac{2R_r^2\theta^2 p_m}{\rho_s h\left(\omega^2\theta^2 + 1\right)}\left\{\frac{1}{\omega\theta}\sin\omega t - \cos\omega t + e^{-t/\theta}\right\} . \quad (5.20d)$$

The new variable ϕ is defined as

$$\phi = \sqrt{\omega^2 - (\beta/\theta)^2} . \quad (5.21)$$

In the coupled case, the dimensionless number β may be thought of an FSI parameter indicating the degree to which the motion of the vessel affects the fluid pressure [6]. The condition $\beta = 0$ corresponds to an infinitely thick vessel, and $\beta = \infty$ corresponds to a massless vessel, that is, a free surface. Stated differently, β increases linearly as a function of fluid density, fluid sound speed, and the characteristic time of the shock wave and decreases linearly as a function of shell density and shell thickness ($R_r^2/h = 1/h - 1/R + h/\left(4R^2\right) \approx 1/h$ for $h \ll R$). Similarly, $\omega^2\theta^2$ is a dimensionless number expressing the ratio of elastic to vessel inertial forces. The relative importance of fluid pressure and elastic forces may be readily gauged by examining the magnitude of the terms in the $\left(\omega^2\theta^2 - 2\beta + 1\right)^{-1}$ factor in Eq. (5.20). For the Jumbino experiment, $\omega^2\theta^2 = 0.484$ and $2\beta = 0.073$.

Time-histories of hoop strain and vessel energy are shown in Figs. 5.3 and 5.4 for both the coupled and uncoupled cases. During the period of initial expansion ($t \le 0.086$ ms $\equiv t_m$), the maximum strains are 5.09 x 10^{-4} and 5.52 x 10^{-4} (8.4% difference) and the maximum vessel energies are 7.068 x 10^4 and 8.312 x 10^4 bar-cm^3 (17.6% difference). The percentage differences compare well with the 7.7% and 15.8% values given by the acoustic wave transmission model [Eqs. (5.10)-(5.12)]. These modest differences are what one expects given that β is small and that $p_{uncoupled}$ is modestly greater than $p_{coupled}$ (Fig. 5.2) over this time interval. But this is only half the story.

After t_m, the vessel energy stays nearly constant in the uncoupled case but falls steadily in the coupled case. To understand this difference in behavior, consider the two p(t) curves in Fig. 5.2. In the coupled case—which captures FSI—the shell returns energy to the water as evidenced by a rise in p(t) for $t_m < t < 0.15$ ms. In contrast, the uncoupled p(t), in falling exponentially, offers a decreasing resistance to the inward motion of the shell; hence, little energy is lost from the vessel for $t > t_m$.

In summary, we considered fluid-structure interaction in the above analysis from an energy transmission perspective subject to the ability to model the fluid shock wave as an acoustic wave. Subjecting a thick-walled vessel to an idealized shock wave and considering vessel dynamics in just one dimension, we observe significant changes in vessel energy and strains when FSI is not adequately modeled. Two dimensionless numbers, β and $\omega^2\theta^2$, indicate the relative magnitudes of fluid, elastic, and inertial forces. The parameter β, which captures the influence of five problem variables, is seen to be useful for gauging the importance of FSI. The physical mechanisms discussed in this section for a simple p(t) are useful in Section VI, where a two-dimensional motion is computed and p(t) is more complex.

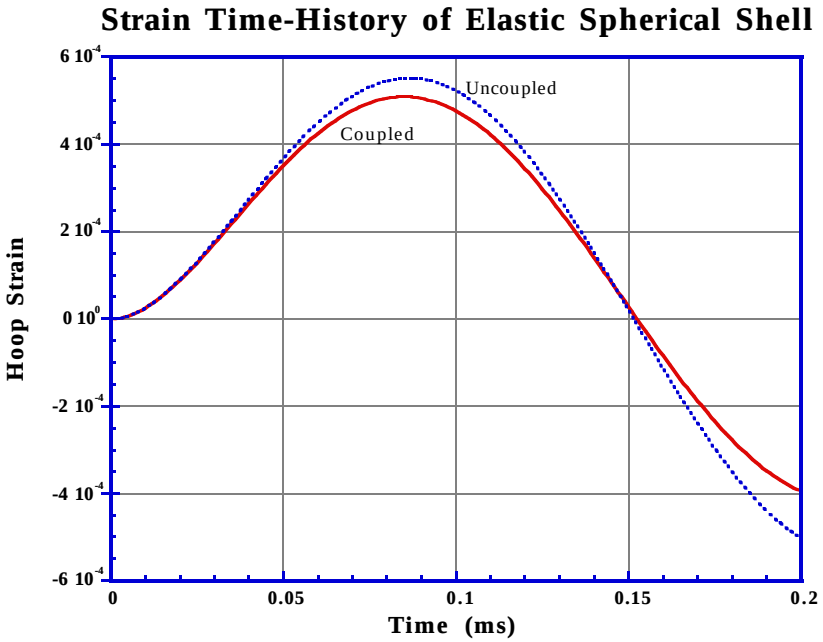

Fig. 5.3
Hoop strain for coupled and uncoupled cases.

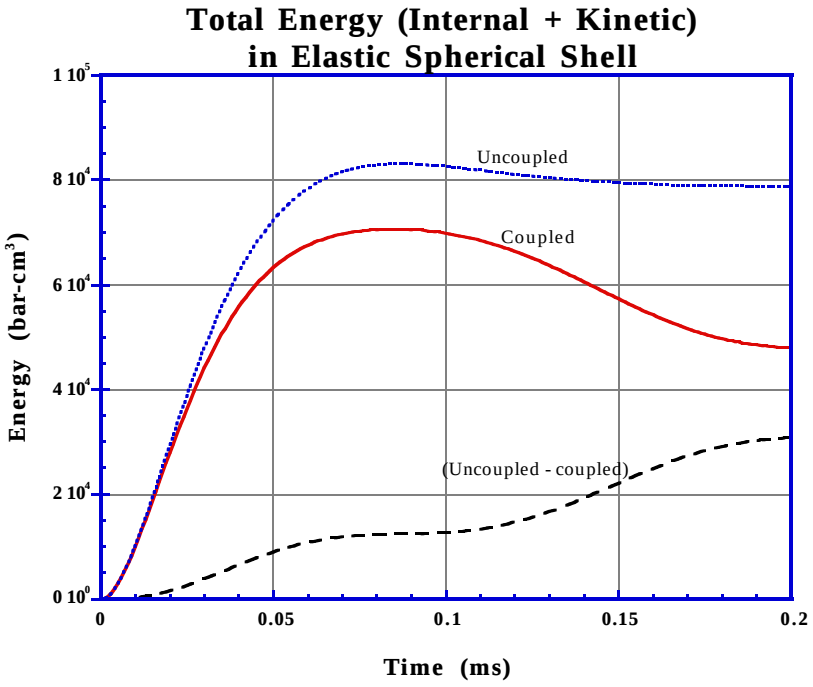

Fig. 5.4
Vessel energy for coupled and uncoupled cases.

VI. TWO-DIMENSIONAL FSI CALCULATIONS AND EXPERIMENTAL RESULTS

In this section we describe the results of the Jumbino experiment and compare them with a pair of two-dimensional numerical simulations. In Sections VI.A and VI.B is a description of the time and space dynamics of the coupled calculation. Comparison and analysis follow in Sections VI.C and VI.D. Unless noted otherwise, reported quantities are for the coupled calculation.

A. Fluid Time Evolution. The dynamics of the problem are driven by the high explosive. During the time period of interest the bubble expands, contracts, and then expands again as a function of its own energy and the momentum of the surrounding water (Fig. 6.1). In turn, the motion of the water is then affected by resistance and motion of the Jumbino vessel. During the initial bubble expansion the water motion is outward nearly everywhere; during the subsequent bubble contraction the water motion is inward nearly everywhere.

In the first 0.310 ms, the high temperature and pressure HE cylinder rapidly expands 112-fold at an average rate of 20 cm/ms to its maximum size, a nearly spherical gas bubble with a radius of 7.9 cm (V = 2042 cm^3). During this time the temperature and pressure drop from 2714 K and 152.7 kbars to 300 K and 15 bars, driving a quasi-spherical shock into the surrounding water. The water shock reflects off the vessel wall, generating peak pressures of about 680 bars (t = 0.190 ms). The expanding bubble generates a second pressure wave that reaches the wall at t = 0.420 ms, producing peak pressures of about 450 bars. The bubble expands until t = 0.310 ms,

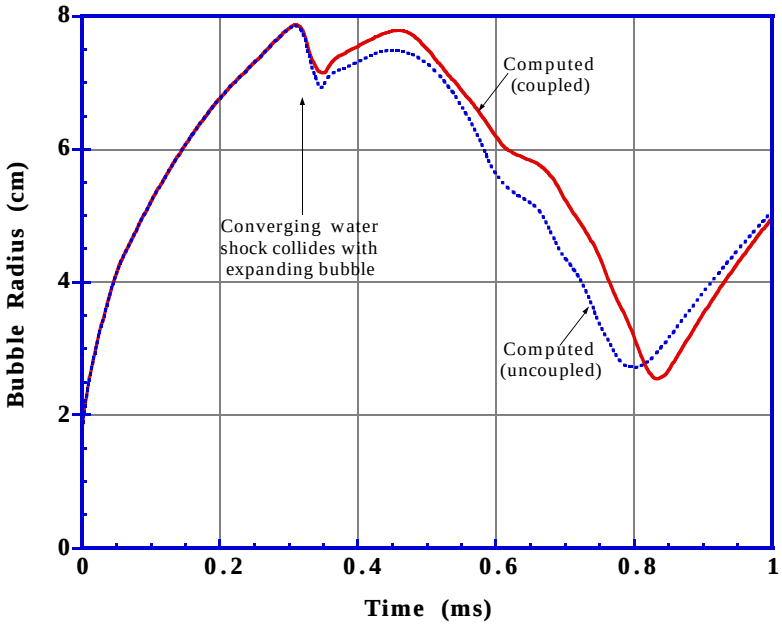

Fig. 6.1
HE-gas bubble radius.

contracts briefly when hit with the now converging first shock, re-expands until t = 0.458 ms, and then collapses because the water is moving inward nearly everywhere.

Away from the port [the Plexiglas covered opening at the top of vessel (Fig. 2.3)] the flow remains approximately spherical until the problem end time (t = 1.0 ms). Figure 6.2 shows the pressure at the vessel wall at the time of the first and second maxima on the equator. Away from the port, p vs. ϕ for the first shock is spherically symmetric; that is, the top curve in Fig. 6.2 should be horizontal. For the fluid mesh used here (Fig. 4.1), an expanding spherical wave first traverses a ϕ-dependent thickness of square mesh cells before reaching the outer cylindrical mesh. The dip in p ($-35° < \phi < +35°$) is thus an artifact of mesh geometry. Although a smoother mesh would produce a more nearly one-dimensional solution, the asymmetry of the present calculation (6% at the equator) is not large enough to alter the principal dynamics of interest here.

On the north axis ($r \approx 0$, $z > 0$). At midradius the water accelerates to a maximum velocity of 6.1 cm / ms (t = 0.100 ms, r = 15 cm), and the shock front reaches the top of the circular port at t = 0.200 ms. Water is pushed through the port opening during the next 0.8 ms at an average rate of 1.9 cm / ms, giving a net mass egress of 588 g at t = 1.0 ms.

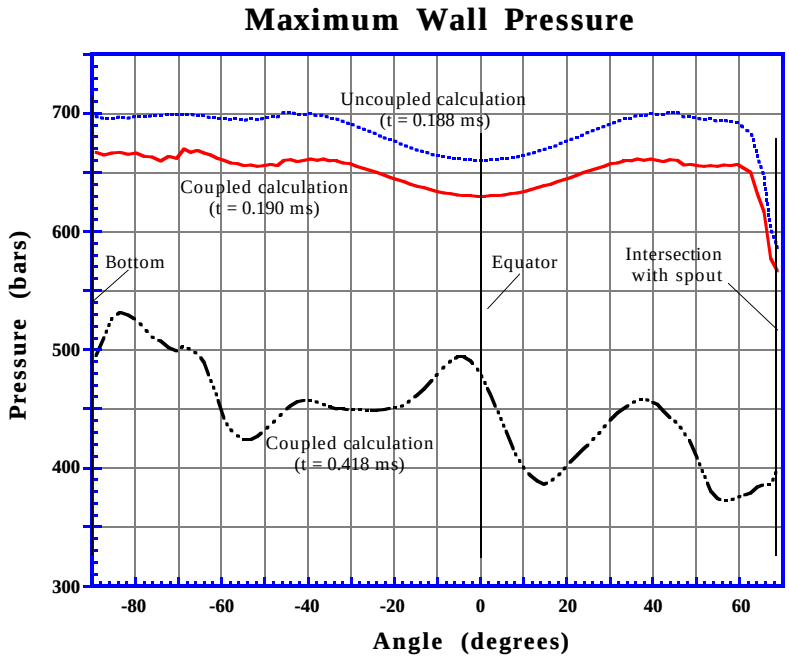

Fig. 6.2
Fluid pressure at the vessel wall
(at the time of maxima on the equator).

On the equator ($r > 0$, $z \approx 0$). At midradius the water accelerates to a maximum velocity of 6.1 cm / ms (t = 0.100 ms, r = 15 cm), and the shock front reaches the wall at t = 0.160 ms, compressing the water to a maximum pressure of 630 bars (t = 0.190 ms). The second pressure pulse—the surge of water ahead of the bubble—compresses the water adjacent to the wall to a maximum pressure of 484 bars (t = 0.418 ms). The water flow then reverses, recompressing the gas, and then expands again. The wall pressure then falls to $p < 1$ bar (t = 0.690 ms), where it remains for the rest of the calculation. In the experiment, cavitation probably occurs but is not modeled in FSI2D. In response to the two fluid pressure waves, the primary vessel vibration mode is radial.

Figure 6.3, which shows the pressure time-history of the fluid adjacent to the vessel wall at $\phi = 0$, is typical of other wall locations.

Away from the r and z axes. The nearly spherical initial shock loads the walls of the vessel nearly uniformly. At later times the flow becomes less spherical because of mesh geometry and outflow at the top.

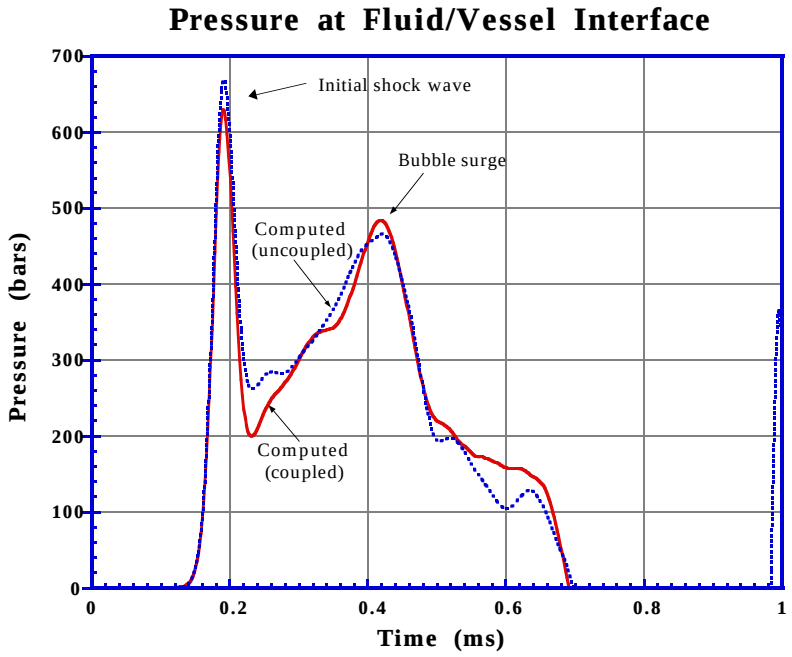

Fig. 6.3
Fluid pressure at the vessel wall (z = 0).

B. Vessel Time Evolution. The primary dynamical response of the vessel is radial—a sequence of expansions and contractions initiated by the nearly spherical internal shock and maintained by a balance of fluid pressure and elastic forces. Three maxima are observed in the outward motion of the vessel with outward radial displacements at the equator of 0.0165 cm (t = 0.275 ms), 0.0133 cm (t = 0.518 ms), and 0.0053 cm (t = 0.774 ms). The motion of the fluid and the vessel are clearly coupled until t = 0.7 ms as evidenced by sustained wall pressures above 100 bars. For t > 0.7 ms sufficient relief, caused mostly by the bubble contraction and to a lesser degree by water egress, allows the remaining water to move around without forced contact with the vessel.

C. Comparison of Measured and Computed Vessel Strains. Typical strain time-histories, at (ϕ = -45°, θ = 0°), are shown in Figures 6.4 and 6.5. A complete set of ε vs. t plots is given in Appendix C. Each plot shows the measured values (M) and the coupled (C) and uncoupled (U) computed values.

The time scale is keyed to the calculated values where the HE detonation occurs at t = 0. The measured values lag the computed values by 0.060 ms at the +ϕ locations and by about 0.020 ms at -ϕ locations. For purposes of comparison, all measured values were shifted by -0.060 ms. The shifted measured values are thereby time aligned to the calculated values for +ϕ plots but precede the computed values by

about 0.040 ms for -ϕ plots. This variation suggests that the actual HE location may have been a bit below the vessel center.

Generally, the calculated strains compare well with the measured values. Analysis of the hoop strain data reveals the observations that follow. Unless noted otherwise, values are averages over all nine data locations.

1. The computed peak-to-peak timing is very nearly the same as the measured values on all plots, a fact which indicates that the FSI model adequately models the timing of the hydrodynamics and the hoop forces in the vessel.

2. All measured-uncoupled-coupled (MUC) traces show the initial expansion caused by the first shock, contraction to near the original radius, re-expansion caused by the bubble surge, and a third peak. The time between the second and third peaks, 0.287 ms, compares well with the estimated natural period of the vessel, 0.253 ms (see Appendix D). Times corresponding to peak strains are listed in Table 6-1.

Table 6-1
Peak Strain Timing

	t_1	t_2-t_1	t_2	t_3-t_2	t_3
Measured	0.280	0.232	0.512	0.271	0.784
Uncoupled	0.281	0.233	0.514	0.287	0.801
Coupled	0.284	0.233	0.517	0.277	0.796

Note: The values $\{t_1, t_2, t_3\}$ are the times (ms) of the three prominent peak hoop strains observed in the ε-t data.

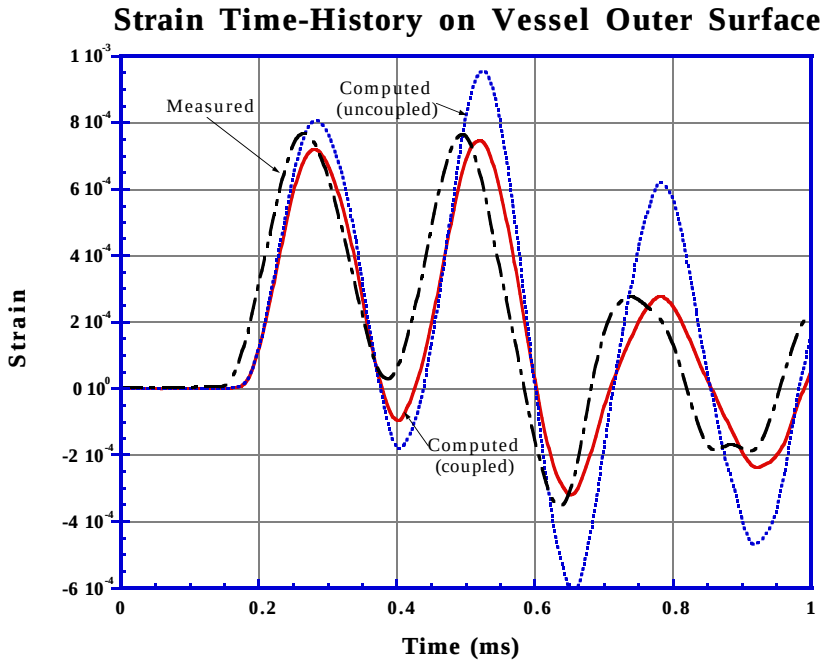

Fig. 6.4
Hoop strain at ϕ = -45° and θ = 0°.

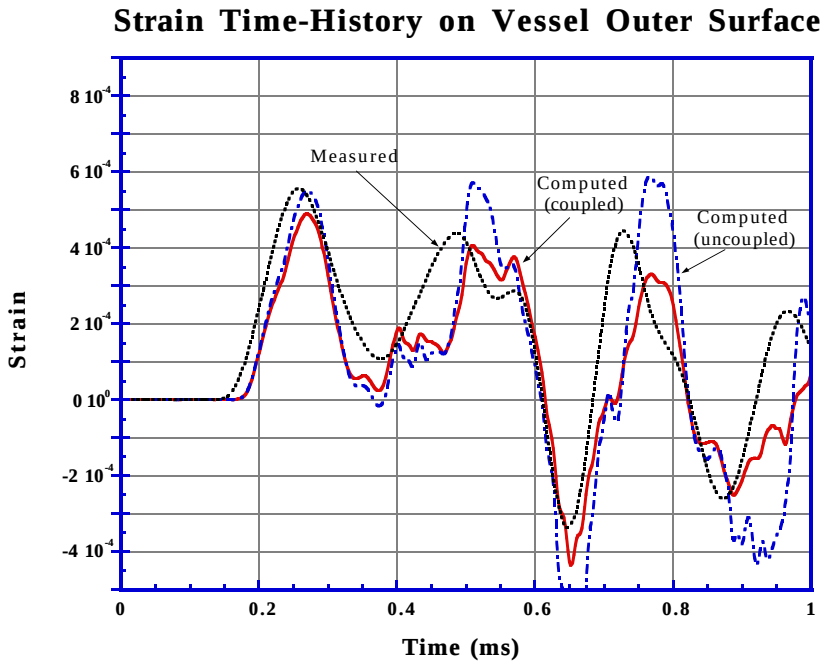

Fig. 6.5
Longitudinal strain at ϕ = -45° and θ = 0°.

3. All MUC traces show that peak strains are smallest on the equator and get progressively larger away from the axis. The traces also correlate between plus and minus ϕ locations. The dip in $p(\phi)$ wall pressure loadings centered around $\phi = 0$ (seetop two curves in Fig. 6.2) accounts for some of this behavior in the computed results.

4. During the first oscillation, the uncoupled strains compare better with the measured values than do the coupled strains; however, the reverse is true at later times. An explanation for this turnaround is offered in Section VI.D. For the time up to the first peak and for a short time thereafter, the dynamics are almost purely one-dimensional and unaffected by the complex interaction and reflection of shocks that occur later and by the vessel vibration modes excited by asymmetric structural boundary conditions.

5. After t_1, uncoupled strains are damped *less* than the coupled and measured values; this is especially notable for $t > 0.6$ ms. The reason for this difference in damping becomes clearer if we consider the time-dependent energy balance in the elastic vessel (Section VI.D).

Generally speaking, these trends are also evident in the longitudinal strain data (Figures 6.5 and C-8 through C-14). The longitudinal waveforms have more structure because (a) there is additional mass at the poles and (b) the vessel is clamped to the support frame at the poles. The major dynamical effect is to lower longitudinal strains (compare with hoop strains) and to introduce higher frequencies into the longitudinal motion. The latter is especially apparent for the computed values.

D. Vessel Energy. For the coupled calculation, Fig. 6.6 shows the internal and kinetic energies of the vessel as a function of time. The vessel energies are due to the mechanical work done by the fluid on the vessel wall (lower curve). During the loading period ($t < 0.7$ ms) the vessel oscillates twice as is readily apparent in the two prominent cycles in the internal energy and pdV work curves. After $t = 0.7$ ms, fluid pressure at the surface is essentially zero and no further energy is exchanged between the fluid and vessel; hence, the pdV curve is constant.

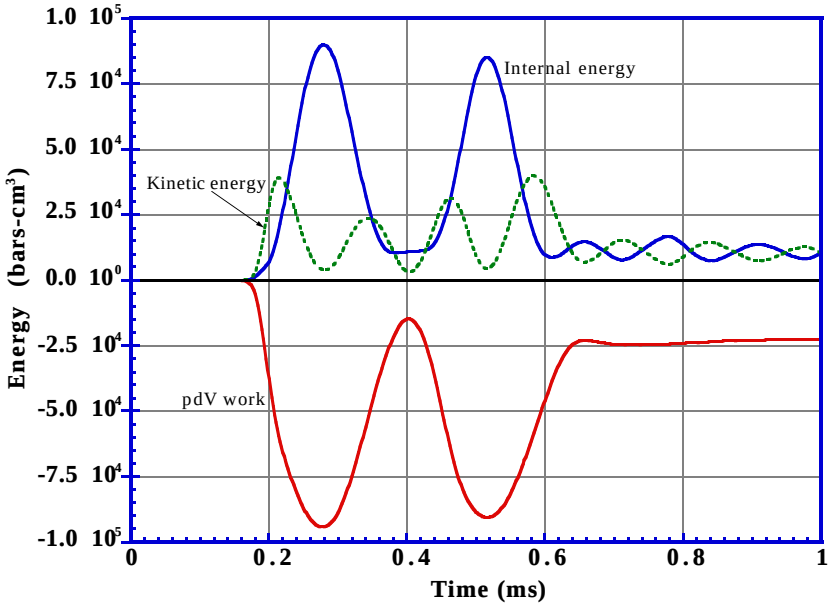

Fig. 6.6
Structural energy balance for coupled calculation.

The total vessel energies (internal + kinetic) are plotted in Fig. 6.7 for both cases. The difference between the uncoupled and coupled calculations (δE_t) is shown in the bottom curve. For $t < t_m$, p(t) is the initial shock wave and δE_t increases steadily—in much the same manner as in the one-dimensional case considered in Section V.C (see Fig. 5.3). For later times, p(t) is a complicated function of wave interactions and FSI; moreover, it is not at all apparent from looking at the two p(t) curves (Fig. 6.3) what form of δE_t to expect. During the first vessel contraction, δE_t actually decreases, nearly compensating for all the previously accumulated error. However, during the second oscillation, δE_t increases on both expansion and contraction so that by the time p(t) = 0, the steady-state vessel energy for the uncoupled case is nearly 3 times the coupled energy. Thus, we expect steady-state stresses to differ by approximately a factor of $\sqrt{3}$.

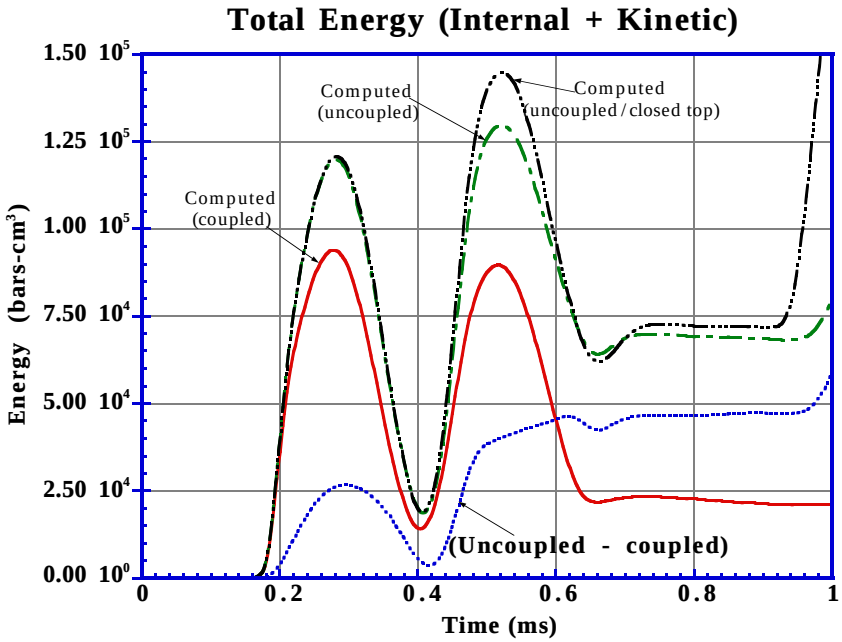

Fig. 6.7
Total structural energy for coupled and two uncoupled calculations.

For the Jumbino experiment, the large differences in late-time vessel energy are the most dramatic illustration of the importance of modeling fluid-structure interaction in a fully coupled manner, compared with a more traditional uncoupled treatment. Even though the uncoupled strains are closer to the measured values (which are assumed to be accurate) than are the coupled strains during the first oscillation, the accumulation of nonphysical energy causes the uncoupled values to diverge significantly from the measured values at later times (see the time-history plots in Appendix C). An uncoupled method is always nonconservative, and the vessel will acquire nonphysical energy for any p(t) scenario of the general type considered here.

VII. CONCLUSIONS

In this report we have examined the dynamical response of a water-filled spherical steel vessel, having a nominal radius of 34.8 cm, a wall thickness of 6.1 cm, and a fundamental period of 0.253 ms, subjected to a centrally detonated 30 g charge of C-4 high explosive. The resultant pressure loading in the range of a few hundred bars lasted 0.550 ms and pushed the vessel radially outward about 0.02 cm, generating peak strains of about 6 x 10^{-4}. Vessel hoop strain time-histories computed by the FSI2D hydrodynamics code compared well with experimental data.

Our computational analysis focused on the fluid-structure interaction aspects of the problem, specifically, on two models. The first model treats the motion of the fluid and solid together in a physically based manner giving a fully *coupled* solution. The second model—the *uncoupled* case—computes the fluid field with a rigid wall

boundary condition. The resulting fluid pressure at the wall is then applied to the vessel as a boundary condition. The coupled model conserves momentum and energy, continuously exchanging both quantities between the fluid and solid during vessel expansion and contraction. The uncoupled model, by contrast, does none of these things.

The uncoupled loading resulted in a nonphysical accumulation of energy in the vessel as evidenced by strain traces that were less damped than and diverged from experimental traces. After the pressure loading, the steady-state vessel energy in the uncoupled model was three times greater than the coupled vessel energy.

Simple one-dimensional models gave results consistent with the two-dimensional calculations. A dimensionless number β that appears in an analytic solution for the vessel motion is a useful parameter for gauging the importance of FSI, particularly with respect to the effect of vessel motion on fluid pressure.

ACKNOWLEDGMENT

The authors would like to thank Wildon Fickett for assistance in understanding detonation physics. His help led to the improved formulation of the BKW-gas equation of state.

APPENDIX A
PROPERTIES OF C-4 HIGH EXPLOSIVE

1 Introduction

C-4 explosive was used in the Jumbino experiment and modeled in the FSI calculations with a BKW-gas high-explosive equation of state (see Appendix B);

$$p = \rho RT(1 + xe^{\beta x}) \quad . \tag{A-1}$$

In this appendix several properties of C-4 are given, including those necessary for modeling the explosive in the computer calculations.

2 Properties

Unexploded density: $\rho_o = 1.65\ g/cm^3$

Composition: 91% RDX, 5.3% TNT, 2.1% polyisobutylene, 1.6% motor oil [9]

Chemical formula: $C_{1.82}H_{3.54}N_{2.46}O_{2.51}$ [9]

Formula weight: 100.0 g

Heat of formation: $(H_f)_{298,1bar} = 3.33$ kcal/mole [5]

Enthalpy: 12.5548 kcal/formula weight = 0.125548 kcal/g at T = 300 K

Detonation velocity: $D_{CJ} = 0.837$ cm/μs [9] (0.811 cm/μs [5])

Detonation pressure: $p_{CJ} =$ 257 kbar [9] (276 kbar [5])

3 Calculated Enthalpy of Explosive at T = 300 K

The BKW code requires that the energy of the explosive, E_o, be based on an enthalpy of formation from elements at T = 0 K, p = 0. Dobratz [9] gives $(H_f)_{298,1bar}$ = 3.33 kcal/mole; thus,

$$E_o = (H_f)_{298,1bar} + \sum_i n_i\left(H^o_{298} - H^o_o\right)_i - p_o v_o = 12.5548 \text{ kcal/formula wt.} \tag{A-2}$$

($e_o = 0.125548$ kcal/gm), where the evaluation of summation terms is shown in Table (A-1).

Table A-1
Calculated Enthalpy of C-4 Constituents

Element	**atoms per form. wt.**	**n, moles per form. wt.**	$H^{o}_{298} - H^{o}_{o}$ **kcal/mole**	$n\left(H^{o}_{298} - H^{o}_{o}\right)$ **kcal/formula wt.**
C_{solid}	1.82	1.82	0.269	0.4896
H_2	3.54	1.77	2.024	3.5825
N_2	2.46	1.23	2.072	2.5486
O_2	2.51	1.255	2.075	2.6041
Total				9.2248

APPENDIX B
BKW-GAS HIGH-EXPLOSIVE EQUATION OF STATE

1 Introduction

The MFICE-2D code that computes the fluid dynamics portion of the FSI calculation described in this report uses a Becker-Kistiakowsky-Wilson (BKW) equation of state to simulate the thermodynamics of the gaseous detonation products that follow a high-explosive burn. Details of the high-explosive burn are not modeled. The BKW-gas model is adequate for transmitting momentum and energy to the surrounding fluid (water) when detailed HE burn-water physics is not needed. In this appendix we describe the BKW-gas model (BKW for short), the procedure used to set the initial gas temperature consistent with the energy of the explosive, the parameters used to model C-4 explosive, and the constant-volume burn values computed by the BKW code [10].

2 BKW-Gas Equation of State

The gaseous high-explosive detonation products are modeled with the BKW equation,

$$p = \rho RT(1 + xe^{\beta x}) = \rho RT F(x), \tag{B-1}$$

where

$$x = \rho \kappa V_c / [\hat{M}(T + \theta)^{\alpha}] \tag{B-2}$$

and

$$F(x) \equiv \left(1 + xe^{\beta x}\right). \tag{B-3}$$

The right side of Eq. (B-1) is composed of an ideal gas component, ρRT, and a non-ideal gas component, $\rho RT(xe^{\beta x})$, called the imperfection term. In the MFICE algorithm Eq. (B-1) is used to compute the pressure in computational cells after the cell values of ρ and T have been advanced. All other variables in Eq. (B-1) are constant for each problem. Determining the initial (t = 0) values, ρ_i and T_i, is the focus of the next section.

3 Adiabatic Constant-Volume Combustion

At t = 0, ρ_i and T_i are set on a portion of the computational domain, V_i, corresponding to a volume as close to the unexploded volume as is practical, to simulate fully reacted products. For consistency we require that the initial mass and energy in V_i be the same as that of the HE. Density ρ_i is computed directly from geometry. To find T_i we imagine the HE is burned (detonated) adiabatically in a

closed volume. To find the final gas product temperature and heat of combustion, we make the following modeling assumptions:

1. The equation of state for the gases is given by Eq. (B-1).
2. The thermodynamic state of the solid HE is known.
3. The product constituents may be computed; hence, we are able to write the chemical reaction $\mathbf{R} \Rightarrow \mathbf{P}$.
4. The volume does not change during combustion (dv = 0).
5. The combustion process is adiabatic (q = 0); that is, no heat enters or leaves the system during combustion.

3.1 First Law of Thermodynamics. The fundamental relationship between work, heat, and internal energy may be written on a mass basis as

$$q = e - w \tag{B-4}$$

or

$$dq = de - dw \tag{B-5}$$

or

$$dq = de + p\,dv. \tag{B-6}$$

For constant volume combustion, dv = 0; for an adiabatic combustion, dq = 0 and Eq. (B-6) becomes

$$de = 0 \tag{B-7}$$

or

$$e_{\mathbf{P}} - e_{\mathbf{R}} = 0. \tag{B-8}$$

3.2 Internal Energy. Equation (B-8) may be rewritten as

$$e_{\mathbf{P}}(T, v, \lambda = 1) - e_{\mathbf{R}}(T_o, v_o, \lambda = 0) = 0, \tag{B-9}$$

signifying T and v as the independent variables and to note that the solid explosive is unreacted ($\lambda = 0$) and that the products are completely reacted ($\lambda = 1$). Eq. (B-9) is the focus of this development, and in the following description, subscripts **P** and **R** will be omitted, $e_{\mathbf{R}}(T_o, v_o, \lambda = 0)$ will be written as e_o, and functional dependency will be included only where needed.

The dependence of internal energy on volume is given by the thermodynamic relation

$$\left(\frac{\partial e}{\partial v}\right)_T = T\left(\frac{\partial p}{\partial T}\right)_v - p \ . \tag{B-10}$$

Following the development by Mader [5], Eq. (B-10) is integrated to give an expression for e(T,v),

$$e(T,v) = e(T,v^*) + \int_{v^*}^{v} \left[T\left(\frac{\partial p}{\partial T}\right)_v - p \right] dv \quad . \tag{B-11}$$

For purposes of clarification, e_P will be expressed in terms of gas and solid components:

$$e(T,v) = e_g(T,v^*)y_g + e_s(T,v)y_s \ , \tag{B-12}$$

which in turn are composed of ideal and imperfect (nonideal) parts. Here, y_g and y_S are gas and solid mass fractions. In the limit $v^* \to \infty$, Eq. (B-11) may be written for a gas as

$$e_g = \frac{1}{\hat{M}} \sum_i \frac{x_i}{\bar{x}} \left[\left(H_T^o - H_o^o \right) - \Re T + H_o^o \right]_i + e_g' \ , \tag{B-13}$$

where

$$e_g' = \alpha R T^2 \frac{F(x) - 1}{T + \theta} \tag{B-14}$$

is the imperfection term. Similarly, Eq. (B-11) for solid products becomes

$$e_s(T,v) = \frac{1}{m_s} \left\{ \left(H_T^o - H_o^o \right)_s + \left(H_o^o \right)_s - p_o V_s^o + e_s' \right\} \ , \tag{B-15))}$$

where

$$e_s' = \int_{V_s^o}^{V_s} \left[T \frac{\partial p}{\partial T} - p \right] dv \tag{B-16}$$

is the imperfection term.

Additional details about the derivation of Eqs. (B-13)-(B-16) and the solution of the chemical equilibrium equations required to compute x_i are given by Mader [5] in his Appendix E.

4 Solution of BKW Equations

4.1 Input Parameters. Because C-4 is mostly RDX, the empirical constants (α, β, κ, and θ) for RDX will be used. These constants and covolumes for the detonation product species, k_i, as suggested by Mader [5], are listed in Table B-1.

Table B-1
Basic BKW Modeling Parameters for C-4

Symbol	Description	Numerical value
α	BKW constant	0.5
β	BKW constant	0.16
κ	BKW constant	10.9097784436
θ	BKW constant	400.0
k	H_2O covolume	250.0
k	H_2 covolume	180.0
k	O_2 covolume	350.0
k	CO_2 covolume	600.0
k	CO covolume	390.0
k	NH_3 covolume	476.0
k	H covolume	76.0
k	NO covolume	386.0
k	N_2 covolume	380.0
k	OH covolume	413.0
k	CH_4 covolume	528.0
k	C_{solid} covolume	0.0

4.2 Numerical Solution. The BKW code computes the detonation properties of an explosive using the BKW equation of state. Solving Eq. (B-9) yields a solution that partitions the mass and energy of the explosive between the gas and solid detonation products. However, because the fluid dynamics in FSI2D models only the gas phase, we instead solve

$$e_{gas}(T, v_{gas} = v_o) - e_o = 0 \qquad \text{(B-17)}$$

subject to the constraint

$$\rho_{gas} = \rho_o \,, \qquad \text{(B-18)}$$

thus ensuring that the mass and energy of the explosive are conserved in the FSI model.

We modified the BKW code to solve Eq. (B-9) for T when v is known, that is, for an adiabatic constant-volume burn. Eq. (B-9) and the equilibrium equations are solved iteratively until successive approximations for T (T^k and T^{k+1}) differ by less than 10^{-3} degrees. For $v = v_o$ and considering only gas phase products [Eqs. (B-17) and (B-18)],

the solution is T_i = 2714.16 K, compared with T_i = 2558.09 K when the detonation products are partitioned between gas and solid phases. The differences in e and p in the two solutions for 300 ≤ T ≤ 5000 K are shown in Figs. B-1 and B-2.

Thermodynamic properties of product species are computed as follows.

H_o^o	Joint Army-Navy-Air Force (JANAF) tables
$H_T^o - H_o^o$	Polynomial curve fits to JANAF data
$e_s'(T, v)$	Cowan solid equation of state [11]

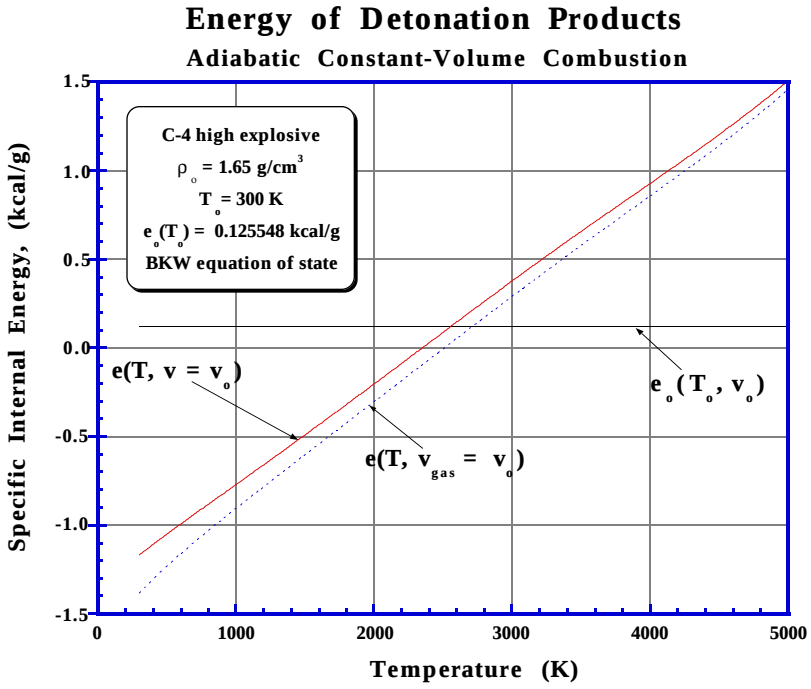

Fig. B-1
Values of e(T, v_o) computed with Eq. (B-9) and a BKW equation of state.

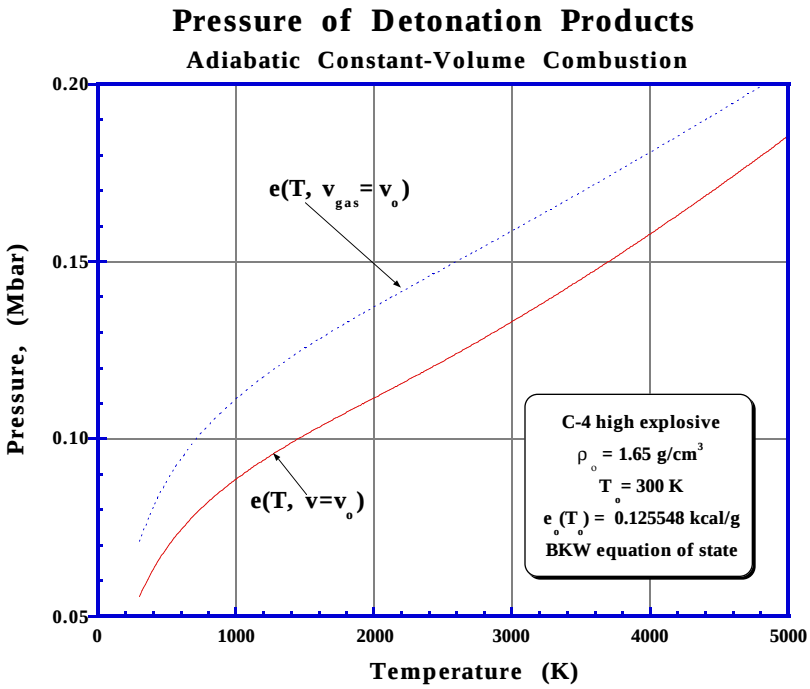

Fig. B-2
Values of $p(T, v_o)$ corresponding to those of $e(T, v)$ computed from Eq. (B-9).

4.3 Output Parameters. The detonation properties of C-4 as computed by the BKW code solution of Eq. (B-17) and subject to the constraint of Eq. (B-18) are given in Tables B-2 and B-3.

Table B-2
Properties of Detonation Products

Property	Value
T	2714.16 K
p	0.1526948 Mbar
ρ	1.7757 g/cm^3
ρ_{gas}	1.6500 g/cm^3
ρ_{solid}	2.8555 g/cm^3
$\hat{M}$	24.33826 g/mole
R	3.457277 bar-cm^3/g-K
V_c	333.83

Table B-3
Composition of Detonation Products
(100 g of C-4)

Species	Moles
H_2O	1.76552120010E+00
H_2	2.07806756277E-03
O_2	2.88426227019E-07
CO_2	3.21927271803E-01
CO	1.00594084160E-01
NH_3	1.29558918861E-03
H	2.50752373712E-06
NO	2.82346953878E-05
N_2	1.22933808806E+00
OH	1.36058503752E-06
CH_4	2.27707249266E-04
C_{solid}	1.39725093679E+00

APPENDIX C
STRAIN TIME-HISTORY PLOTS

Azimuthal (hoop) and meridional (longitudinal) strains were measured at nine locations on the exterior of the Jumbino vessel. Figures C-1 through C-7 show the measured hoop strains and the corresponding coupled and uncoupled computed values. Figures C-8 through C-14 show the longitudinal strains at these same locations, with the exception of Figure C-8, for which the θ = 0° strain data were unavailable.

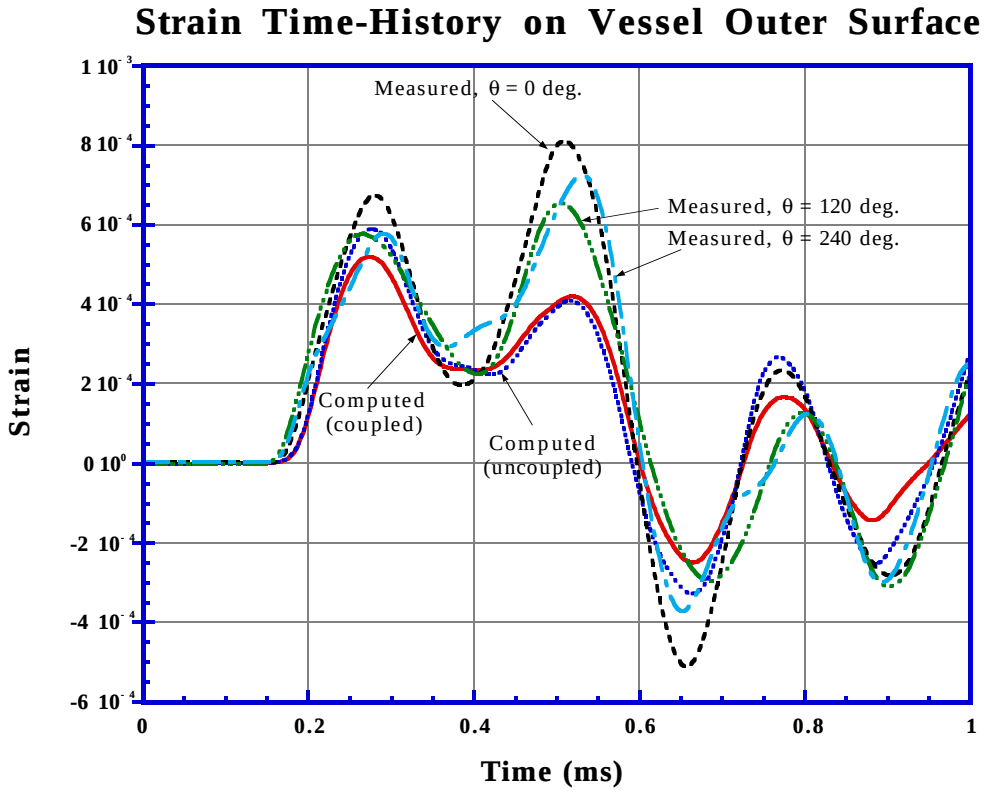

Fig. C-1
Hoop strain at ϕ = 0°, θ = 0°, 120°, and 240°.

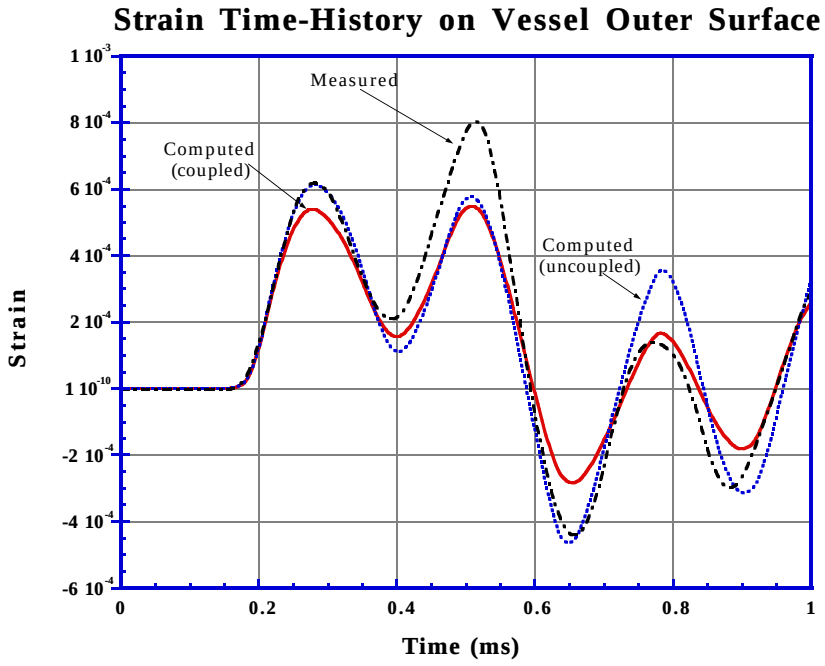

Fig. C-2
Hoop strain at ϕ = +15° and θ = 0°.

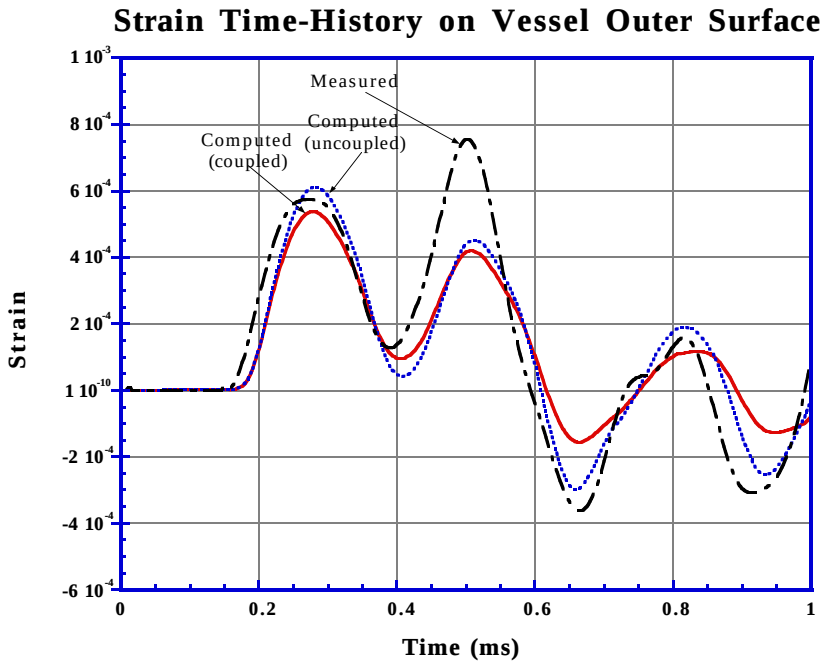

Fig. C-3
Hoop strain at ϕ = -15° and θ = 0°.

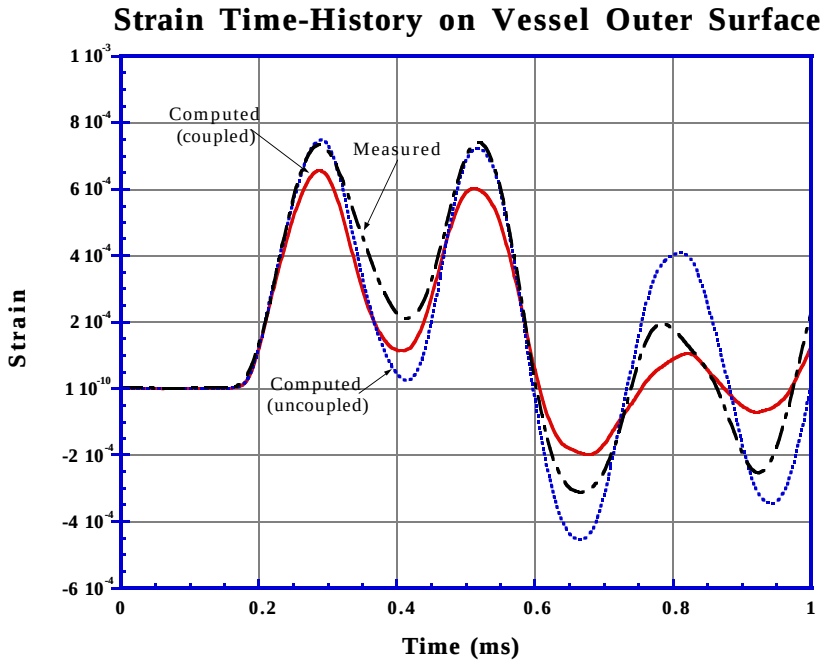

Fig. C-4
Hoop strain at ϕ = +30° and θ = 0°.

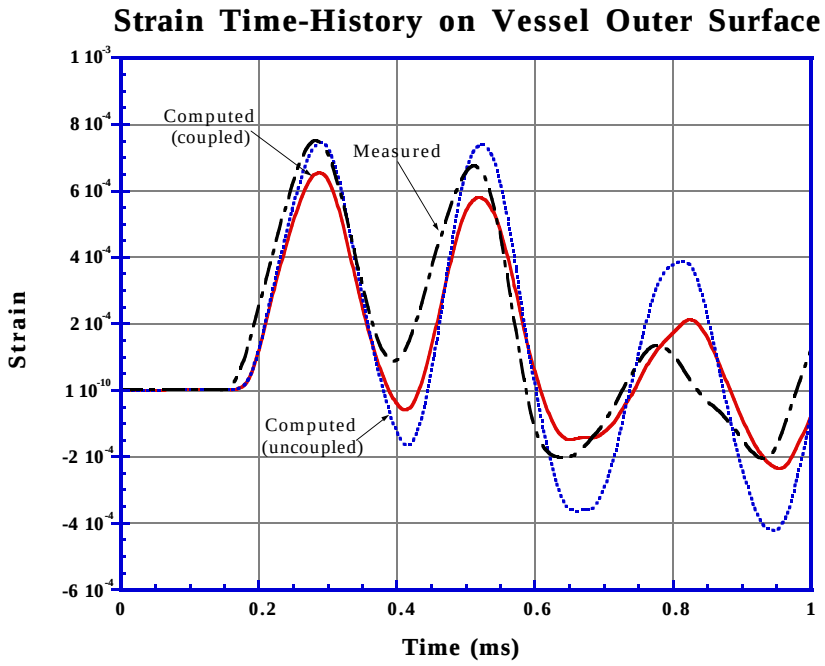

Fig. C-5
Hoop strain at ϕ = -30° and θ = 0°.

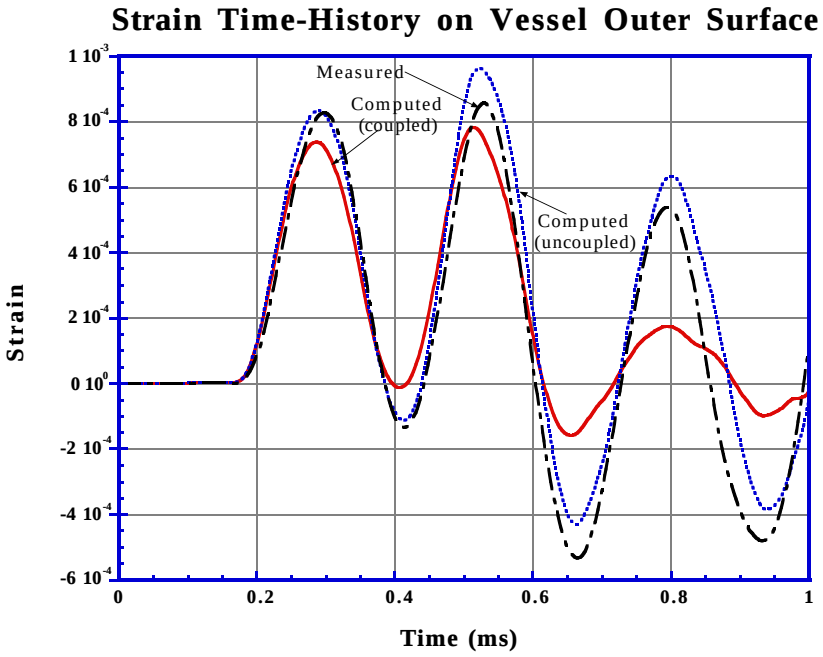

Fig. C-6
Hoop strain at ϕ = +45° and θ = 0°.

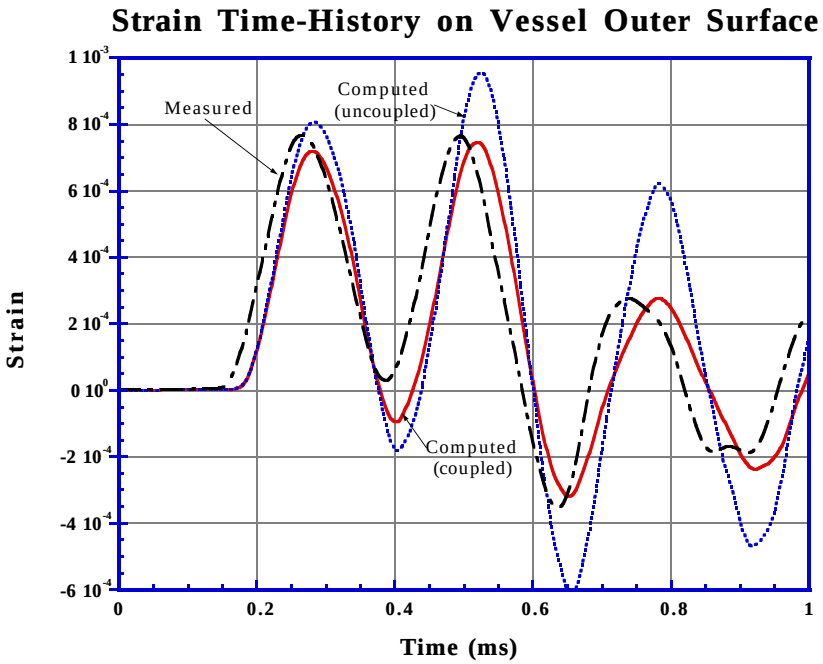

Fig. C-7
Hoop strain at ϕ = -45° and θ = 0°.

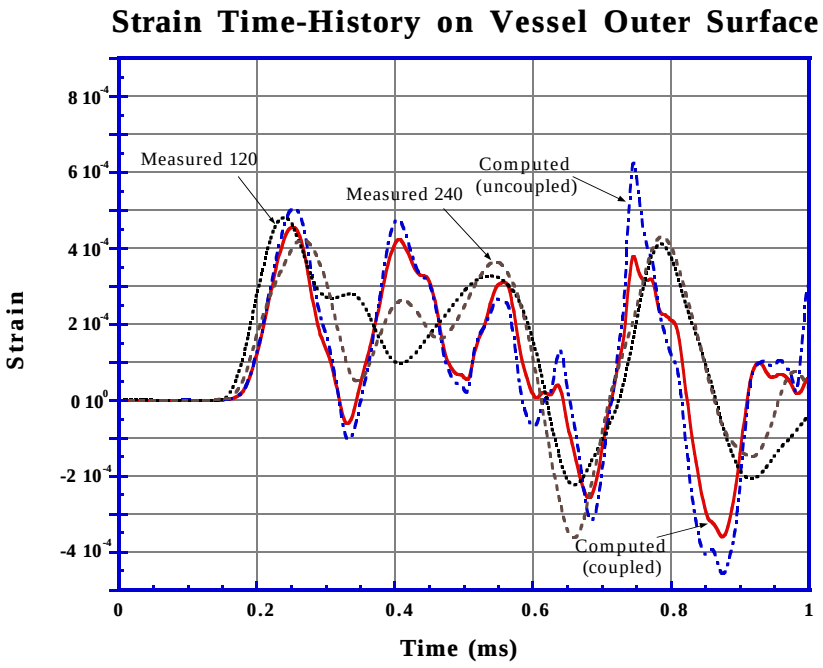

Fig. C-8
Longitudinal strain at $\phi = 0°$, $\theta = 120°$ and $240°$.

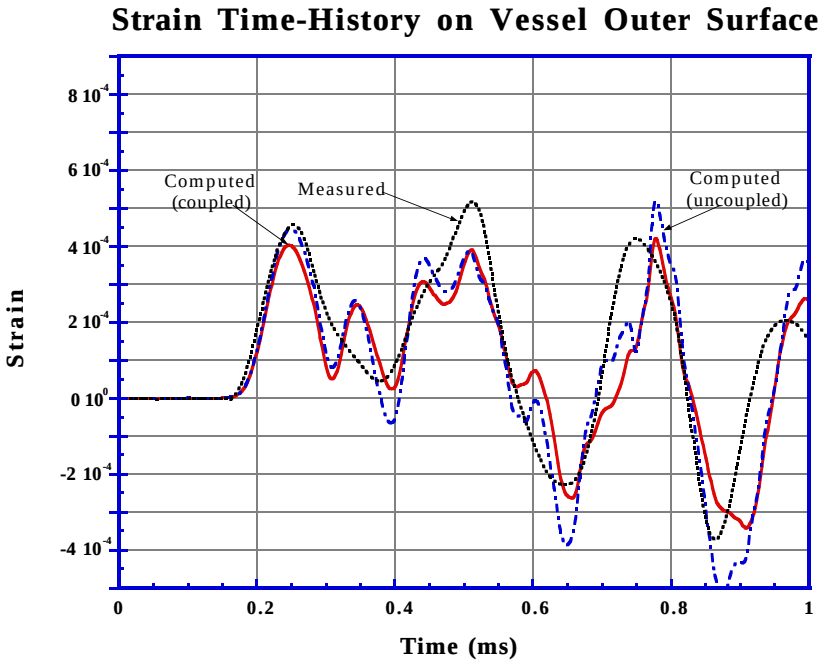

Fig. C-9
Longitudinal strain at ϕ = +15° and θ = 0°.

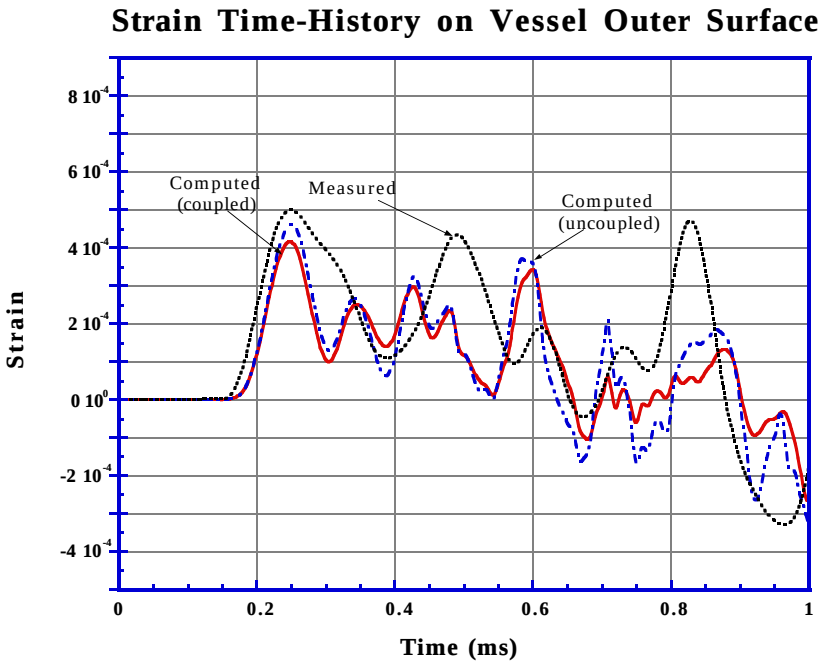

Fig. C-10
Longitudinal strain at ϕ = -15° and θ = 0°.

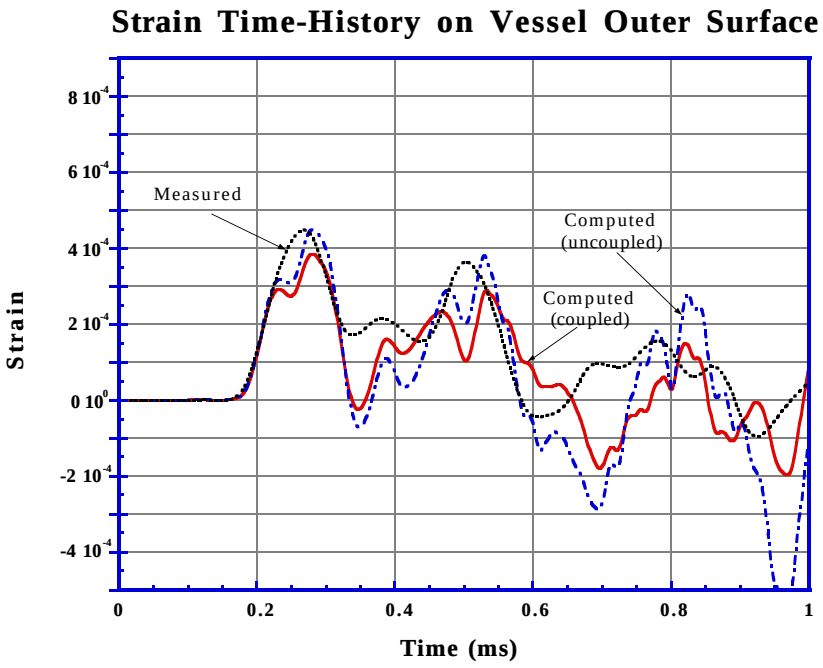

Fig. C-11
Longitudinal strain at ϕ = +30° and θ = 0°.

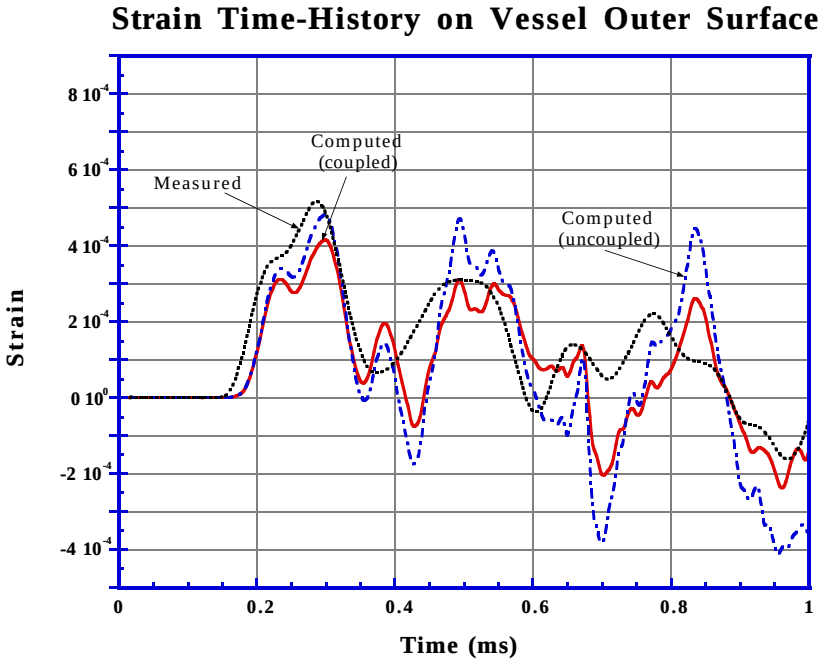

Fig. C-12
Longitudinal strain at ϕ = -30° and θ = 0°.

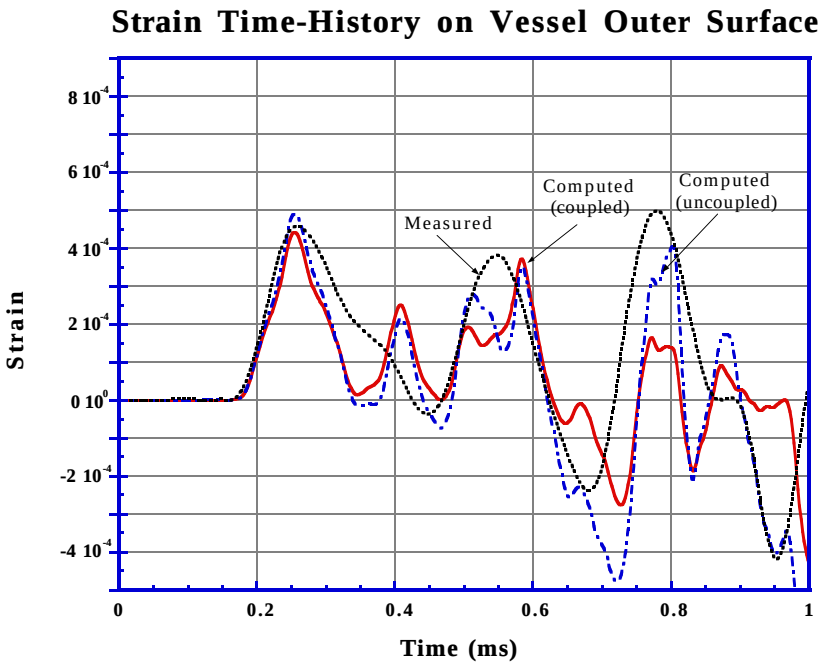

Fig. C-13
Longitudinal strain at ϕ = +45° and θ = 0°.

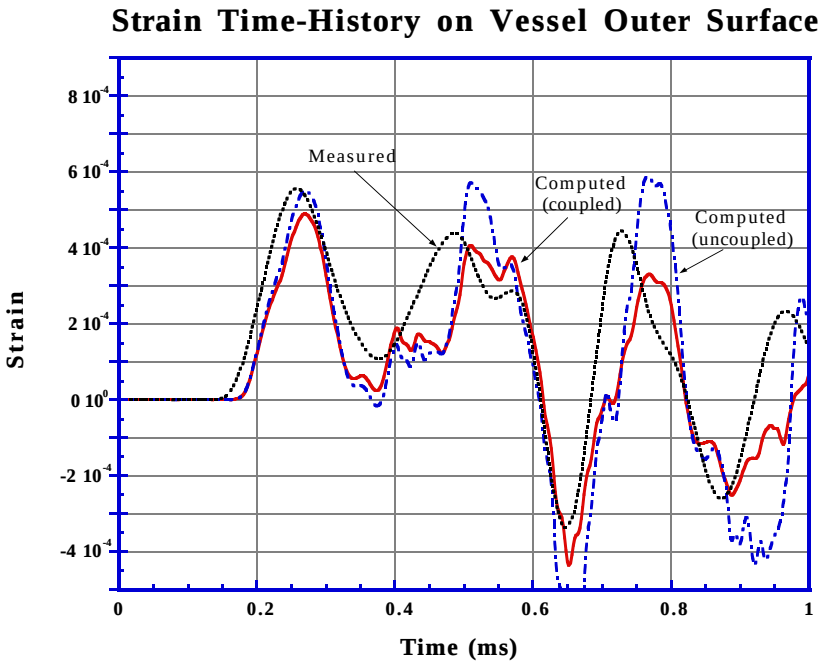

Fig. C-14
Longitudinal strain at ϕ = -45° and θ = 0°.

APPENDIX D
FUNDAMENTAL MODE VIBRATION OF A THICK-WALLED SPHERE

The theoretical fundamental frequency for a thin-walled spherical vessel is

$$\omega = \sqrt{\frac{2Y}{\rho\left(R^2 + \frac{h^2}{12}\right)(1-\nu)}}, \tag{D-1}$$

where ω is the fundamental frequency in radians/second, Y is the Young's modulus of elasticity, ρ is the mass density, R is the mean radius, h is the wall thickness, and ν is the Poisson's ratio. Using the material constants previously reported in this report, an inner diameter of 24.975 inches and an outer diameter of 29.805 inches (corresponding to an R of 13.695 inches and h of 2.415 inches), we calculated a fundamental frequency of 3.951 kHz (a period of 253 microseconds). One would not expect this to be a good approximation to the thick-walled sphere fundamental frequency, because the ratio, R/h, is 5.67. This ratio is usually limited to greater than 10 for thin-walled theories to apply.

We addressed this issue by calculating the fundamental frequency of a thick-walled spherical vessel. To estimate this frequency, we assumed a displacement field consistent with the response. The displacement field chosen is one due to a static pressure difference between the outside and inside of the sphere. This is a spherically symmetric field of the form

$$s(r) = C\left[\frac{a^3}{4r^2G} + \frac{r}{3K}\right], \tag{D-2}$$

where s is the radial displacement, r is the radius to a point, C is a constant (or a time-varying value for the following analysis), *a* is the outer radius of the sphere, G is the shear modulus of the material, and K is the bulk modulus of the material.

Let us assume a sinusoidal form for C:

$$C = A\ \sin(\omega t), \tag{D-3}$$

where *A* is a constant, ω is the frequency of vibration, and *t* is time. To calculate the maximum kinetic energy associated with this mode of vibration, we must integrate the following:

$$\begin{aligned} KE_{max} &= \max_{t<\infty} \int_R \frac{1}{2}\rho \dot{s}^2 dV = \int_{r=b}^{r=a} 2\pi\rho r^2 \omega^2 A^2 \left(\frac{a^3}{4r^2G} + \frac{r}{3K}\right)^2 dr \\ &= 2\pi\rho\omega^2 A^2 \left[\frac{a^5}{16G^2}\left(\frac{a}{b} - 1\right) + \frac{\left(a^5 - b^5\right)}{45K^2} + \frac{a^5}{12KG}\left(1 - \frac{b^2}{a^2}\right)\right] \quad , \end{aligned} \tag{D-4}$$

where b is the inner radius of the sphere.

The maximum strain energy associated with this mode of vibration is obtained by integrating

$$SE_{max} = \int_R \frac{1}{2}\sigma{:}e \; dV = 2\pi A^2 \left[\frac{a^3}{4G}\left(\frac{a^3}{b^3} - 1\right) + \frac{a^3 - b^3}{3K} \right], \qquad \text{(D-5)}$$

where σ and e are the stress and strain tensors compatible with the displacement function chosen and elastic response.

Using the Rayleigh method, we equate the maximum kinetic energy with the maximum strain energy and solve for ω, the natural frequency. This gives us

$$\omega^2 = \frac{1}{\rho} \frac{\dfrac{a^3}{4G}\left(\dfrac{a^3}{b^3} - 1\right) + \dfrac{a^3 - b^3}{3K}}{\dfrac{a^5}{16G^2}\left(\dfrac{a}{b} - 1\right) + \dfrac{\left(a^5 - b^5\right)}{45K^2} + \dfrac{a^5}{12KG}\left(1 - \dfrac{b^2}{a^2}\right)} . \qquad \text{(D-6)}$$

Using Eq. (D-6) and the values already mentioned for inner and outer radii and material constants, the fundamental frequency is calculated to be 4.013 kHz or a fundamental period of 249 microseconds. This is remarkably close to the frequency estimate from thin-walled theory (within 2%).

The effect of added mass. If water (density of 1 g/cm^3) is added inside the sphere, it is expected that the stiffness of the water will not have much influence on the frequency of the sphere. The mass of the fluid, however, will tend to lower natural frequencies as is observed with submerged structures. This is commonly referred to as an "added mass" effect—the modal mass is increased, leading to a lower frequency.

How much does the mass added to the structure by the water lower the fundamental frequency of the sphere? The sphere has a mass of 728.9 kg. The mass of water inside the sphere is 133.7 kg. The lowest value we can expect the frequency to attain is determined from the following equation:

$$\omega_{\text{added mass}} = \sqrt{\frac{\text{Original Modal Mass}}{\text{Original Modal Mass} \; + \; \text{Modal Mass of Water}}} \geq \sqrt{\frac{728.9}{728.9 + 133.7}}\omega \cong 0.92\omega . \qquad \text{(D-7)}$$

From this, we can see that the frequency of the coupled fluid-structure sphere will be reduced by at most 8%.

NOMENCLATURE

c_o	ambient sound speed in water, 148.3 cm / ms
c_v	specific heat capacity at constant volume, ergs / g-K
e	total specific internal energy
e_g	specific internal energy of gas
e_o	specific enthalpy of undetonated HE at T = 300 K
e_s	specific internal energy of solid
e'_s	imperfection specific internal energy of solid
e'_g	imperfection specific internal energy of gas
H^o_T	molar enthalpy at temperature T, ergs / mole
H^o_o	molar enthalpy of formation from elements at reference state (T = 0 K, p = 0), ergs / mole
F(x)	$\equiv (1 + xe^{\beta x})$, BKW equation-of-state multiplier
h	sphere wall thickness, 6.134 cm
i	gas species
K	bulk modulus
M	molecular weight, g / mole
$\hat{M}$	molecular weight of BKW gas, g / mole
m	mass, g
m_s	mass of solid, g
P	products
p	pressure, bars
p_o	ambient pressure, bars
q	heat, ergs / g
r	radius, cm
R	gas constant, $R = \Re / M$
R	mean radius of sphere, $(R_i + R_o)/2 = 34.875$ cm
R_i	inner radius of sphere, 31.7185 cm
R_o	outer radius of sphere, 37.852 cm
R	reactants
$\Re$	acoustic impedance; universal gas constant, 8.31441×10^7 ergs / (mole-K) = 8.31441×10^7 g-cm^2 / (s^2-mole-K)
s	vessel radial displacement, cm
T	temperature, K
t	time, ms
t_m	time of vessel's first maximum expansion, ms

u	vessel radial velocity, cm/ms
V	volume, cm^3
v	specific volume, cm^3/g
V_c	covolume, cm^3
V_s	volume of solid explosive products, cm^3
V_s^o	initial volume of solid explosive products, cm^3
v_o	$1/\rho_o$, cm^3/g
v_t	total specific volume, $v_t = v_g + v_s$, cm^3/g
W	explosive charge weight, g
w	specific work, ergs/g
x_i	number of moles of specie i
$\bar{x}$	total number of moles of gas
Y	Young's modulus, 2.07×10^6 bars
y_g	gas mass fraction
y_s	solid mass fraction
α	BKW equation-of-state constant (0.5 for C-4)
β	BKW equation-of-state constant (0.16 for C-4)
ε	strain
ϕ	latitudinal angle, diameter
κ	BKW equation-of-state constant (10.9097784436 for C-4)
ν	Poisson's ratio, 0.29
λ	degree of chemical reaction; 0 for no reaction, 1 for complete reaction
θ	characteristic time for shock wave; BKW equation-of-state constant (400 K).
ρ	density, g/cm^3
ρ_o	ambient water density, 1.00 g/cm^3; unexploded density, g/cm^3
ρ_s	vessel density, 7.833 g/cm^3
ω	fundamental frequency, rad/s

REFERENCES

1. B. A. Kashiwa, N. T. Padial, R. M. Rauenzahn, W. B. VanderHeyden, "A Cell-Centered ICE Method for Multiphase Flow Simulations," Los Alamos National Laboratory document LA-UR-93-3922 (rev.), presented at the ASME Symposium on Numerical Methods for Multiphase Flows, Lake Tahoe, Nevada, June 19-23, 1994 .

2. B. A. Kashiwa, R. M. Rauenzahn, "A Multimaterial Formalism," Los Alamos National Laboratory document LA-UR-94-771, presented at the ASME Symposium on Numerical Methods for Multiphase Flows, Lake Tahoe, Nevada, June 19-23, 1994.

3. L. M. Taylor and D. P. Flanagan, "PRONTO2D: A Two-Dimensional Transient Solid Dynamics Program," Sandia National Laboratories report SAND86-0594 (March 1987).

4. M. W. Lewis, B. A. Kashiwa, R. W. Meier, and S. Bishop, "Nonlinear Dynamic Fluid-Structure Interaction Calculations with Coupled Finite Element and Finite Volume Programs," presented at the ASME Winter Annual Meeting, Chicago, Illinois, November 6-11, 1994, Los Alamos National Laboratory document LA-UR-94-2443.

5. C. L. Mader, *Numerical Modeling of Detonations* (University of California Press, Berkeley, 1979).

6. R. H. Cole, *Underwater Explosions,* (Princeton University Press, Princeton, 1948).

7. J. Roth, "Underwater Explosions," in *Encyclopedia of Explosives,* PATR 2700, **10**, S. M. Kaye, ed. (ASAARDC, Dover, New Jersey, 1983).

8. M. M. Swisdak, Jr., "Explosion Effects and Properties: Part II—Explosion Effects in Water," Naval Surface Weapons Center report NSWC/WOL TR 76-116 (February 1978).

9. B. M. Dobratz, "LLNL Explosives Handbook: Properties of Chemical Explosives and Explosive Simulants," Lawrence Livermore National Laboratory report DE85-015961 (March 1981).

10. C. L. Mader, "FORTRAN BKW: A Code for Computing the Detonation Properties of Explosives," Los Alamos Scientific Laboratory report LA-3704 (May 1967).

11. R. D. Cowan and W. Fickett, "Calculation of the Detonation Products of Solid Explosives with the Kistiakowsky-Wilson Equation of State," J. Chem. Phys. **24**, 932 (1956).

Los Alamos
NATIONAL LABORATORY
Los Alamos, New Mexico 87545